Fabrication and Characterization of SnO$_2$-MoS$_2$ based nano-composite electron transport layer for Perovskite Solar Cell

By

Muhammad Salik Qureshi

Reg. No. 00000320754

Session 2019-21

Supervised by

Dr. Nadia Shahzad

US-Pakistan Center for Advanced Studies in Energy (USPCAS-E)

National University of Sciences and Technology (NUST)

H-12, Islamabad 44000, Pakistan

August 2023

Fabrication and Characterization of SnO$_2$-MoS$_2$ based nano-composite electron transport layer for Perovskite Solar Cell

By
Muhammad Salik Qureshi
Reg. No. 00000320754

Session 2019-21

Supervised by
Dr. Nadia Shahzad

A Thesis Submitted to the US-Pakistan Center for Advanced Studies in Energy in partial fulfillment of the requirements for the degree of
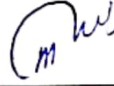
MASTER of SCIENCE
in
Energy Systems Engineering

US-Pakistan Center for Advanced Studies in Energy (USPCAS-E)
National University of Sciences and Technology (NUST)
Islamabad, Pakistan
August 2023

Certificate

This is to certify that work in this thesis has been carried out by **Mr. Muhammad Salik Qureshi** and completed under my supervision in Solar Energy Research Laboratory, U.S.-Pakistan Center for Advanced Studies in Energy, National University of Sciences and Technology, H-12, Islamabad, Pakistan.
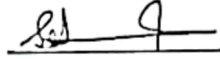
Supervisor:

Dr. Nadia Shahzad
USPCAS-E
NUST, Islamabad

GEC member # 1:

Dr. Muhammad Imran Shahzad
USPCAS-E
NUST, Islamabad

GEC member # 2:

Dr. Sehar Shakir
USPCAS-E
NUST, Islamabad

GEC member # 3:

Dr. Naseem Iqbal
USPCAS-E
NUST, Islamabad

HOD-ESE

For
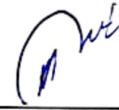
Dr. Rabia Liaquat
USPCAS-E
NUST, Islamabad

Principal

Dr. Adeel Waqas
USPCAS-E
NUST, Islamabad

THESIS ACCEPTANCE CERTIFICATE

Certified that final copy of MS/MPhil thesis written by **Mr. Muhammad Salik Qureshi** having Registration No. **00000320754** of **USPCAS-E** has been vetted by undersigned, found complete in all respects as per NUST Statues/Regulations, is free of plagiarism, errors, and mistakes and is accepted as partial fulfillment for the award of MS/MPhil degree. It is further certified that necessary amendments as pointed out by GEC members of the scholar have also been incorporated in the said thesis.

Signature: _____

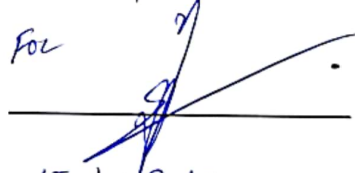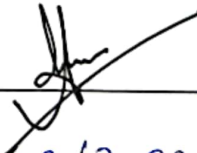Name of Supervisor _____Dr. Nadia Shahzad_____

Date: _____15/08/2023_____

Signature (HoD): _____

Date: _____15/08/2023_____

Signature (Dean/Principal): _____

Date: _____15/08/2023_____

i

Dedication

The thesis is wholeheartedly dedicated to my beloved parents, siblings and especially my friends, in particular Shayan Umar who pushed me forward in times when I struggled. I am thankful for their love and measureless support. You have been a driving force throughout this process. Even when my weak soul was withered, they always saw light in me, if today I am capable to stand up is because they always healed my broken bones. Every single equation and effort are dedicated to you.

.

Acknowledgment

First and foremost, I would like to express gratitude to Allah (SWT), the Almighty God for the blessing, kindness, and inspiration in lending me to accomplish the research work, Without Him, I couldn't stay patient and in control in this research work.

I would like to sincerely thank my supervisor, **Dr. Nadia Shahzad,** for his guidance and support throughout this study, and especially for his confidence in me. His illuminating views, constructive criticism, and consistent feedback made me sail through numerous obstacles that came in the way. I also extend my humble gratitude to all the faculty and GEC members for her unconditional support. I pay special regards to my Parents, siblings, and my friends for their constant encouragement and prayers that have made this endeavor easy and tireless. In the last but not least, I pay special tribute to my mother who forfeited everything to see me successful.

Abstract

Electron transport layer (ETL) plays a crucial role in the performance of perovskite solar cell (PSC). Charged with the task of electron extraction and delivering them to their respective electrode, they play a vital role in enhancing the overall performance of the solar cell (SC). A number of materials, particularly metal oxide (MO) and their composites have been tested for this role. Tin Oxide (SnO_2) and its composites have shown superior properties that have proven crucial for enhancing the performance of SC by improving the charge extraction properties of the layer. Therefore, this paper presents the study of composite of SnO_2 with the pristine nano flakes of Molybdenum Disulfide (MoS_2), a new emerging material for SC application. The addition of 20% (v/v%) MoS_2 in SnO_2 has not only improved the crystallinity of SnO_2 but also resulted in enhanced and larger grain size for perovskite absorber layer. In addition to this, the flakes also cause an increase in charge carrier concentration and conductivity of the film. Furthermore, due to the incorporation of flakes the charge carrier kinetics at the ETL/perovskite interface was also reduced leading to lower recombinations and improved charge transport at the interface indicating that the SnO_2 and MoS_2 composite will be a suitable option as an ETL for development of PSC.

Keywords: SnO_2-MoS_2 composite, electron transport layer, Perovskite solar cell, ambient fabrication

Contents

List of Tables

List of Figures

List of Publications

1. ***M.S. Qureshi***, N. Shahzad, S. Nadeem, S. Mehmood, A. Sattar, N. Iqbal, S. Shakir, M.U. Nawaz, M.I. Shahzad **"To study the optical, electrical and morphological properties of SnO_2-MoS_2 composite based Electron Transport Layer for Solar Cell Application"**.

2. ***M.S. Qureshi***, N. Shahzad, M.A. Tariq, M.U. Nawaz, S. Riaz, M.I. Shahzad **"Fabrication of HTL free Perovskite Solar Cell using Compositional Engineering via Cesium Bromide for Ambient Fabrication"**. Applied Physics Letter (Submitted) (Manuscript#APL-23-AR-08246)

3. A. Sattar, N. Shahzad, M.A. Tariq, T. Yousaf, ***M.S. Qureshi***, M.I. Shahzad, R. Liaquat, M. Ali **"Carbonyl Functional Group Assisted crystallization of Mixed-cation Mixed-halide Tin-Lead Narrow Bandgap Perovskite Absorber in Ambient Conditions"** Applied Physics Letter (Published)

4. S. Umar, W. Tanveer, A. Waqas N. Shahzad, ***M.S. Qureshi***, A.K .Janjua, S. Shakir, M. Dehghan **"A Solar PV Surface-Cleaning Setup to Optimize the Electricity Output of PV modules in a polluted Atmosphere"** Journal of Renewable Energy (Published) (Manuscript # RENE-D-22-06936R1)

5. S. Nadeem, N. Shahzad, S. Mehmood, ***M.S. Qureshi***, A. Sattar, R. Liaquat, S. Shakir, M.I. Shahzad **"Solution-Processed Zn_2SnO_4 / ZTO Electron Transport Layers for Planar Perovskite Solar Cells"** Journal of Materials Science (Under Review) (Manuscript # JMSC-D-23-03092)

6. S. Mehmood S. Nadeem, ***M.S. Qureshi***, A. Sattar, N. Iqbal, R. Liaquat, M.I. Shahzad **"Effect of lanthanum doped SnO_2 on the performance of mixed-cation mixed-halide perovskite for planar PSCs"** Thin Solid Films (Under Review) (Manuscript # TSF-D-23-00511)

7. M.U. Nawaz; N. Shahzad; **M.S .Qureshi**; N. Iqbal; M. Ali; M.I. Shahzad, "**Optimizing optoelectronic properties of Perovskite Absorber Material via ambient compositional engineering with Potassium (K) and Tin (Sn).**", Journal of Photochemistry and Photobiology , A: Chemistry (Submitted)

List of abbreviations

SnO_2……………………………………………………………………Tin Oxide

MoS_2………………………………………………….…Molybdenum Disulfide

FTO………………………………………………………….Florine Doped Tin Oxide

PSC……………………………………………..……….Perovskite Solar Cell

PCE…………………………………………….…Power Conversion Efficiency

ETL…………………………………………….…Electron Transport Layer

HTL…………………………………………….…….Hole Transport Layer

UV-Vis…………………………………………….……….Ultraviolet Visible

XRD…………………………………………….….……….X-Ray Diffraction

SEM………………………………………….….Scanning Electron Microscopy

OM…………………………………………………….……..Optical Microscopy

PL……………………………………………….……….Photoluminescence

$MAPbI_3$………………………………………….……Methylammonium Iodide

CsBr……………………………………………….…………Cesium Bromide

SAL…………………………………………….……Standard Absorber Layer

PAL……………………………………………..….Perovskite Absorber Layer

Chapter 1

Introduction

The following chapter provides a brief introduction to solar energy, its importance and generation. This is followed by the explanation of different types of solar cell technologies with the emphasis on the third generation PSC and electron transport layer. Afterwards, the problem statement is defined along with the objective and proposed research for this thesis.

1.1.   Renewables: Dominant Source of Energy

With the rise in urbanization, increase in dependence and access to electricity and the development in the world the demand of energy is also increasing. The prime resources for the generation of electricity being used over the past few decades are fossil fuels. However, there are some disadvantages that come with the consumption of such fuels. First there are limited resources of fossil fuel available, and the present resources are rapidly depleting. Second, the use of fossil fuels has led to environmental pollution and are not adequate for the sustainable development of human society. With the increasing gap in the demand and supply of the electricity, studies are being focused on to find such sources of energy that not only are able to fill the gap between demand and supply but are also clean, non-depleting and most important sustainable. Therefore, the attention has been shifted towards the renewable sources of energy which possess all the positive attributes and are being integrated into the energy system to not only reduce the dependance from the fossil fuels but also for the sustainable development of the system.

1.2.   Environmental Impact

The consumption and the burning of fossil fuel has been damaging the environment in several ways. First and foremost, the burning of fossil fuels adds up to the emissions of the greenhouse gases (GHG) which includes Methane (CH_4), Sulfur Oxide (SO_X), Nitrous Oxide (NO_X), and most important Carbon Dioxide

(CO$_2$) which makes up approximately 75% of the GHG emissions [1]. All these gases have been contributing to the effect known as Global Warming which has been responsible for the rise in the Earth's temperature. As a result of global warming the earth temperature has been increased up to 1°C from pre-industrialization level and has been increasing at a rate of 0.2°C per decade [2]. In addition to the damaging effect caused to the environment, the fossil fuel utilization has also been harmful to both human health causing diseases like skin cancer, Asthma and Reparatory problems. Phenomena's such as acid rain and smog which are some of the post effects caused by the emissions are also extremely harmful. As a result of such catastrophic effects, there has been rapid deployment and reduction in the price of renewable energy technology worldwide.

1.3. Renewable Energy Resources

With energy demand being on the rise, the production of energy through the conventional sources of energy has caused irreversible damage to the system. The cost of extraction and transportation of conventional resources is also on the rise since the resources are depleting at a fast pace. Therefore, the existence of such situations over a longer period of time are not only alarming as the rates of the fuels will constantly rose but are also harmful for the environment due to the increase GHG emissions. Hence there is constant need of finding such sources of energy that can deliver energy clean energy at lower cost with minimum environmental impact. According to the report of IRENA, the share of the renewable energy in electricity generation in the world will increase up to 55% and will become affordable source of the energy in many countries throughout the world [3].

Renewable energy resources include solar, geo-thermal, biofuel and wind that are acquired from resources that are replenishable from time after time. These resources are available in abundance and an enormous amount of energy can be generated from these resources. They can not only contribute to fill the gap in energy demand but are also environmentally friendly having net zero emissions and are sustainable. Among the present renewable energy resources, solar is one of the best options that is affordable, reliable, low cost and abundantly available (almost 23,000

TW per year.) that can allow us to reduce our dependency on the conventional resources available thus eliminating carbon emissions and global warming.

1.4. Solar Energy

Harvesting energy from the sun is the main form of solar energy. However, there are two alternative methods available to extract energy from the sun. The first one is Solar Thermal Power Generation and the second one is Photovoltaic Solar Generation.

1.4.1 Solar Thermal Power Generation

Solar thermal power generation converts the heat from the sun into electricity by concentrating or reflecting it. the system comprises of two main components. The first one is the reflector which reflects the sunlight on to the second component which is the receiver. The receiver receives the heat and is used to heat up a fluid that is used to produce steam. The steam is then used in the mechanical system to rotate the blades of the turbine. The turbine further runs the generator which in turn produce electrical energy [4].

1.4.2 Solar Power Generation

This is the second method of harvesting the sun's energy and converting it into electrical energy. In this method the solar device converts the incoming photons from the sun into electricity through a process known as Photovoltaic Effect. It can be broadly divided into two steps. In the first step, the device which is being fabricated from semiconductor materials absorbs the incoming photons. These photons excite the electrons from their lower energy state into the higher energy state. In the second step, the electrons in their higher energy state are then transferred into the external circuit so that their energy can be harvested through their motion thus generating current.

1.4.3 How a solar cell work

A solar cell is a device that converts the incoming photons from the sun into electrical energy. The solar cells are made up of semi-conducting materials. Semiconducting materials are those in which instead of having a continuous energy states the energy states are separated by the energy gap. The lower energy state is called Valence Band and the higher energy state is called Conductions Band. The electrons in the conduction band are available to produce electric current. However, the electrons are needed to be excited in the Conduction band to generate electric current. This is done through a process called Photovoltaic Effect which is the operating principle of the solar cells. According to this effect, whenever light falls on the surface of the semiconductor material, it is being absorbed resulting in the generation of the electron-hole pair. This is a metastable state and both excited particles are required to move towards their respective electrodes to harness the energy thus generating both current and voltage. The steps can be summarized as follows [5]:

- Absorption of the incident photons.
- Generation of the electron hole pair.
- Movement of the electron hole pair towards their respective electrode.
- Transfer of electrons into the outer circuit being delivered to load thus generating current.
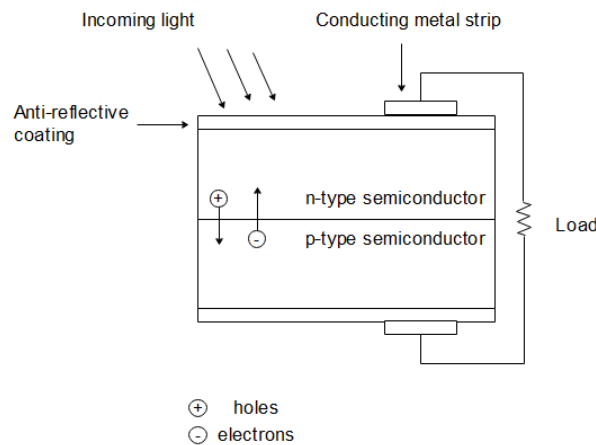
Figure 1.1: Lateral View of a solar cell [6]

4

1.5.   Generation of the Photovoltaic Technologies

Traditionally Silicon was the first and most widely used semi conducting material for the solar cell fabrication. However, with the ongoing research and development, various new semi conducting material developed in addition to Silicon giving rise to the different generation of the Photovoltaic. PV technologies can be divided into three different generation:
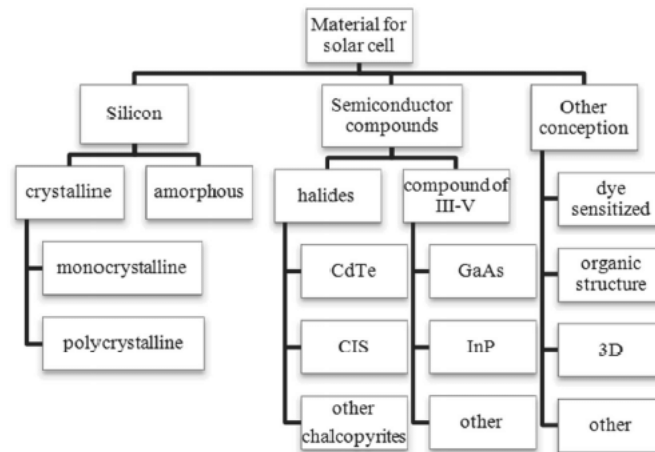
Figure 1.2: Classification of Solar Cells [7]

1.5.1   First generation

The first generation is the oldest PV technology. This generation has been well established and developed in terms of their fabrication processes and technology. Silicon solar cell are the most widely used and manufactured generation of solar cells in the world. Three different types of solar cells belong to this category which includes Single Crystalline, Multi-crystalline and Amorphous. These types of which mainly differ in the type of Silicon used to manufacture them.

1.5.1.1.   Monocrystalline Silicon Solar Cells

They have the highest lab efficiencies of 26.2%. They are made up of cylindrical silicon ingot which is grown from single Silicon crystal. They possess the highest purity in their generation but cost more as compared to the other two.

1.5.1.2. Polycrystalline Silicon Solar Cells

These types of solar cells are made from different crystals of silicon instead of single crystal. Their efficiency is around 21%. They are less efficient as compared to the monocrystalline but also cost less as compared to former one.

1.5.2. Second Generation of Solar Cell

The second generation of the solar cell are called thin film solar cells. Their minimum material usage and low cost have made them attractive for the market. However, their efficiency and lifetime are still lower than as compared to the first generation. The second generation comprises of Amorphous Silicon, Copper Indium Gallium Di-Selenide (CIGS), Cadmium Telluride (CdTe). Amorphous Silicon is the most widely used because they can be made from the first-generation technology. However, being less efficient have led to the development of the CIGS (22.6%) and CdTe (22.1%) [8][9]. Their efficiency ranges between 10.2-22.6% with Amorphous Silicon having the lowest and CIGS having the highest efficiency of 22.6%.

1.5.3. Third Generation of Solar Cell

Having higher cost of the manufacturing for the first generation in addition to issues of toxicity and material availability for the second generation, a third generation of solar cell has been developed. In addition to being novel, they are different from the other two generation because they do not rely on the p-n junction design. Different type of cells who belong to this generation include Organic Photovoltaic Solar cell (OPV), Dye Synthesized Solar Cell (DSSC), Quantum Dot (QD) and Perovskite Solar Cell (PSC). These solar cells have low cost and can easily be prepared.

The highest efficiencies recorded for the PSC till now have been 25.6% while for the DSSC the recoded efficiencies have been 14% [10] and for the OPV the maximum recorded efficiency is 18.07% [11]. Even with such tremendous efficiency, the PSC have been under research phase and research is being focused on to increase their stability, scalability, and efficiency to make them commercial and increase their market share.
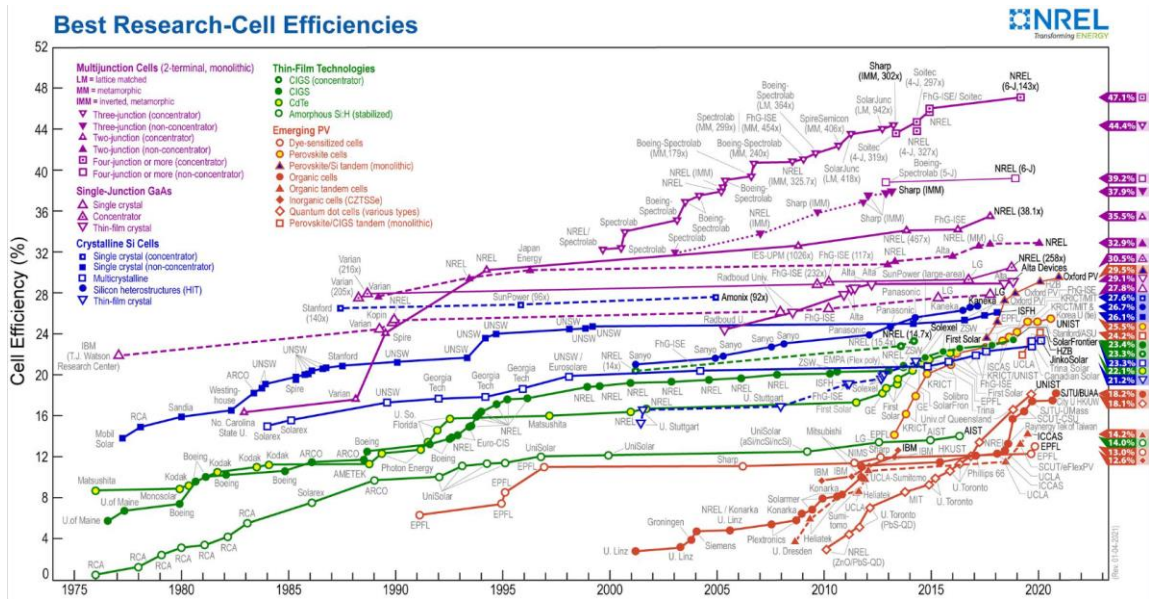
Figure 1.3: Recorded solar cell efficiencies by National Renewable Energy Laboratories (NREL) [12]

1.6.　Perovskite: The advance generation of Solar Cell

PSC belongs to the third category of the solar cell. The word Perovskite is actually a crystal structure which is similar to the mineral called Perovskite consisting of Calcium Titanium Oxide. The general stricture of the Perovskite can be represented by the formula ABX_3 and shown in Figure 1.4 where A is a positively charged cation and occupies the center of the cube, B is also positively charged cation and occupies the corner of the cube while X is an Anion and occupies the faces of the cube.
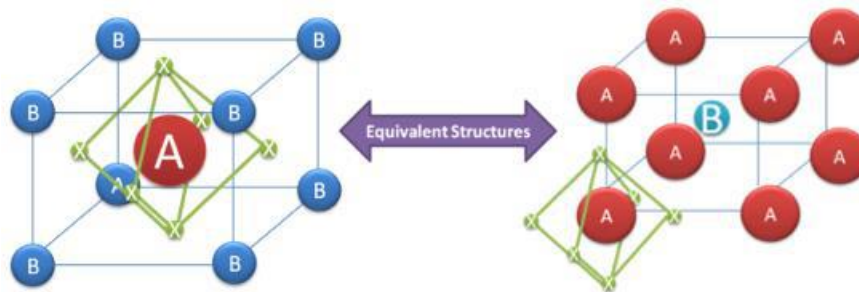
Figure 1.4:Structure of the Perovskite [13]

1.7. Component of Perovskite Solar Cell

Majorly PSC consists of three different layers including Electron Transport Layer (ETL), Perovskite absorber layer (PAL) and Hole Transport layer (HTL). The perovskite absorber is responsible for generation of charges while the charge transport layers are associated with delivering charges to their respective electrode. The current focus is on the ELT while the complete description of these components can be found in Chapter 2.

1.8. Electron Transport Layer

The ETL plays a crucial role in PSC by facilitating the movement of electrons. It serves as a bridge between PAL and electrode while ensuring the seamless flow of electrons. Being in the center of electron injection to transport and collection, it enhances the performance of the device while promoting the charge balance and eventually influencing the overall performance of the cell. There are multiple materials that are used for the role of ETL. The details of some of those can be found in chapter 2. However, for the current study, SnO_2 has been used as ETL.

1.9. Problem Statement

The ETLs in PSC are responsible for playing the crucial role of electron extraction and to support the growth of the perovskite absorber layer. Despite playing its efficient role as ETL, SnO_2 has been accompanied by certain defects such as high temperature processing, defects and trap states and charge mobility limitation [14]–[16] making it difficult for the layer to achieve good efficiency for the solar cell. Therefore, to further improve the properties of existing ETL, surface modification in terms of composite formation is suggested by using SnO_2 composite.

1.10. Objectives

Following are the objectives of the research:

- Fabrication and characterization of SnO_2 based Electron transport layer.

- Embedding the MoS_2 in the SnO_2 layer in different compositions.

- Optimizing the electrical/optical properties of the ETL for the efficient charge extraction from perovskite absorber layer.

1.11. Aim of the Research

Therefore, in this research, a relatively less explored composite of SnO_2 and MoS_2 in field of solar cell has been proposed. The research is aimed to fabricate and characterize the Nanocomposite Electron Transport Layer (NC-ETL) for PSC. The process involves the use of refluxing process for the synthesis of Tin Oxide (SnO_2) in which the flakes of MoS_2 are then further added in different v/v ratios. The samples prepared were deposited via spin coating and were characterized by the XRD, UV-Vis, Hall Effect, SEM, EDX, and PL. For the device fabrication, SnO_2 was used for the cell fabrication and the efficiency was obtained through the I-V curve tracer. The absorber layer was deposited in an ambient condition. Instead of metal contacts and HTL, carbon contacts were deposited with the help of the doctor blading which served both the role of HTL along with contact for charge collection.

Summary

The chapter provides an overview of the energy consumption along with the dominant role of fossil fuel for the energy production since the industrialization era while focusing on the role of renewable sources of energy, their significance, and their sustainability in future. The role of the solar in the energy mix, their advantages and types of Solar Technologies including both the Solar Thermal Power Technology and solar Photovoltaic Technology has been briefly explained. Complete working and operation of the solar cell is also demonstrated. While keeping the solar photovoltaic technology in view, classification of the solar cell is reviewed. The first generation are silicon wafer based and is the most matured technology among all the generations. Second generation are thin film that are cost effective but still less efficient while the third generation are nanostructured based solar cell. Perovskite solar cells belong to this generation and have shown tremendous efficiencies with just a decade of research while showing promising aspects for the future. Furthermore, the problem associated with the ETL leading to poor device performance have been suggested to be improve through surface modification of SnO_2 by suggesting a composite of SnO_2 with MoS_2 along with the fabrication of carbons-based PSC.

References

[1]   M. D. Mastrandrea *et al.*, *IPCC, 2015: Meeting Report of the Intergovernmental Panel on Climate Change Expert Meeting on Climate Change, Food, and Agriculture. World Meteorological Organization, Geneva, Switzerland, 68 pp.*, no. May. Dublin, 2015.

[2]   M. Allen *et al.*, "Chapter 1 — Global Warming of 1.5 ºC." pp. 47–93, 2018.

[3]   IRENA, *Global Renewables Outlook: Energy transformation 2050*. 2020.

[4]   Y. Chu and P. Meisen, "Review and comparison of different solar energy technologies.   http://www.geni.org/globalenergy/research/review-and-comparison-of-solar-technologies/Review-and-Comparison-of-Different-Solar-Technologies.pdf," *Global Energy Network Institute (GENI)*, no. August, pp. 1–56, 2011.

[5]   "Solar   Cell   Structure | PVEducation." https://www.pveducation.org/pvcdrom/solar-cell-operation/solar-cell-structure (accessed Jul. 07, 2021).

[6]   "(a) What is a solar cell? Draw the labelled diagram of a solar cell.(b) Name the semiconductor material which is usually used for making solar cells.(c) Write the uses of solar cells." https://www.vedantu.com/question-answer/a-what-is-a-solar-cell-draw-the-labelled-diagram-class-12-physics-cbse-5fc743b242be3a5ec81c65b4 (accessed Jul. 17, 2023).

[7]   M. Science, "Comparative Study of Cu 2 ZnSnSe 4 Monograin Powder Synthesis in Different Molten Salts Monoterapulbrilise Cu 2 ZnSnSe 4 sünteeskasvatuse võrdlus," 2015.

[8]   M. Powalla *et al.*, "Advances in Cost-Efficient Thin-Film Photovoltaics Based on Cu(In,Ga)Se2," *Engineering*, vol. 3, no. 4, pp. 445–451, Aug. 2017, doi: 10.1016/J.ENG.2017.04.015.

[9]   "Cadmium   Telluride | Department   of   Energy."
https://www.energy.gov/eere/solar/cadmium-telluride (accessed Jul. 07, 2021).

[10]   C. P. Lee, C. T. Li, and K. C. Ho, "Use of organic materials in dye-
sensitized solar cells," *Materials Today*, vol. 20, no. 5, pp. 267–283, Jun. 2017, doi:
10.1016/J.MATTOD.2017.01.012.

[11]   Q. Liu *et al.*, "18% Efficiency organic solar cells," *Sci Bull (Beijing)*, vol.
65, no. 4, pp. 272–275, Feb. 2020, doi: 10.1016/J.SCIB.2020.01.001.

[12]   "Best Research-Cell Efficiency Chart | Photovoltaic Research | NREL."
https://www.nrel.gov/pv/cell-efficiency.html (accessed Jul. 07, 2021).

[13]   "Perovskites Solar Cell Structure, Efficiency & More | Ossila."
https://www.ossila.com/pages/perovskites-and-perovskite-solar-cells-an-
introduction (accessed Jul. 07, 2021).

[14]   W. Ke *et al.*, "Low temperature solution-processed tin oxide as an
alternative electron transporting layer for efficient perovskite solar cells," *J Am
Chem   Soc*,   vol.   137,   no.   21,   pp.   6730–6733,   Jun.   2015,   doi:
10.1021/JACS.5B01994/SUPPL_FILE/JA5B01994_SI_001.PDF.

[15]   C. Wang *et al.*, "High-effective SnO2-based perovskite solar cells by
multifunctional molecular additive engineering," *J Alloys Compd*, vol. 886, p.
161352, Dec. 2021, doi: 10.1016/J.JALLCOM.2021.161352.

[16]   W. Hui *et al.*, "Red-Carbon-Quantum-Dot-Doped SnO2 Composite with
Enhanced Electron Mobility for Efficient and Stable Perovskite Solar Cells,"
Advanced   Materials,   vol.   32,   no.   4,   p.   1906374,   Jan.   2020,   doi:
10.1002/ADMA.201906374.

Chapter 2

Literature Review

The chapter presents a detailed look on the perovskite solar cell, its components, their working, and the working principle of cell. Furthermore, it also describes different types of ETL that are used in PSC. It explores what are the suitable properties that must be present in a suitable ETL, what are the different types of ETL that are being used in PSC, their advantages and disadvantages and why certain type of ETL such as SnO_2 are being the mostly employed ones. Beside this, use of TMD's is also explored in this chapter including their recent use in PSC as ETL and how their effectiveness can be utilized with SnO_2 in terms of composite.

2.1   What is Perovskite Solar Cell

With over a decade of research, Organic inorganic metal halide Perovskite Solar Cell (PSC) has been widely investigated because of their low cost, easy processing, availability of materials, band gap tunability (by changing the metal ions, organic cations, & halide ions), higher absorption coefficient and longer diffusion length of charge carriers [1][2]. As reported by the National Renewable Energy Laboratory (NREL), since their debut in 2009, their efficiencies has been improved from 3.8% to over 25% to the present [3].
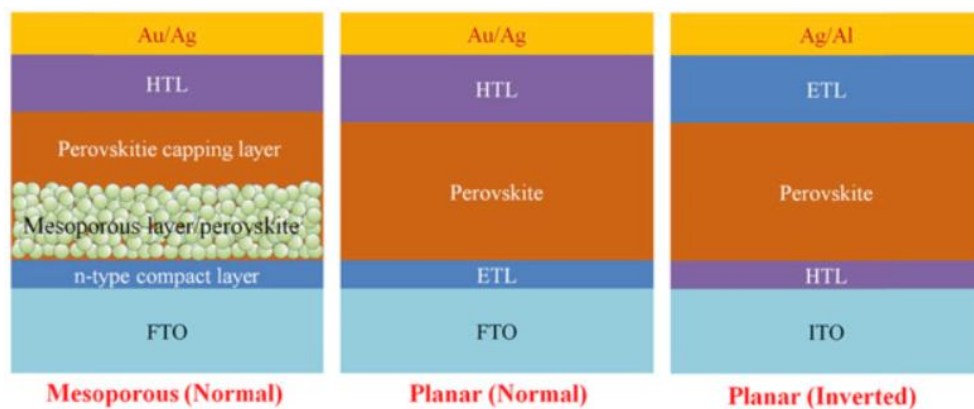
Figure 2.1: Different Architectures of the Perovskite Solar Cell

Among the three generations of solar cells, PSC belongs to the third generation of solar cells. They were initially introduced as the Dyes in the Dye Synthesized Solar Cell (DSSC) from which they closely resemble in their architecture [4]. However, upon knowing about their variety of properties, they have established as a separate class in solar cells and have been widely studied since then. The architecture of the device can be mainly divided into two different classes including Mesoporous and Planar while the latter one being further divided into Normal and Inverted.

2.2 Description of the components in the Perovskite Solar Cell Structure: -

2.2.1 Glass Substrate

These bare glasses act as a substrate upon which the rest of the layers of the cell are deposited.

2.2.2 FTO/ITO

These are classified as Transparent Conductive Tin Oxide (TCO) and the type of glasses which are deposited with materials which not only allow them to be electrically conductive along with along with allowing the light to pass through them.

2.2.3 ETL

It consists of a semiconducting material that are used to transport electrons to their respective electrodes while blocking the movement of holes. A large number of materials have been widely used for the role of ETL with metal oxides being the most prominent one for this role. Most widely used metal oxides are TiO_2, and SnO_2. They are employed in different configurations, sometimes in planar, sometimes in mesoporous or sometimes in the combination of both.

2.2.4 Perovskite Layer

PSC consists of formula ABX_3, where A is the monovalent cation, B is the divalent cation, and X are the halides.
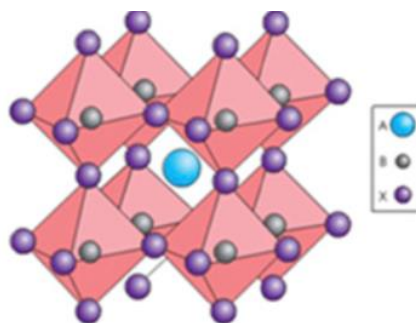
Figure 2.2: ABX_3 structure of the Perovskite

The layer consists of the center of the cell and is used to absorb the incoming wavelength thus generating electron and holes pairs which are then transported to their respective electrodes afterwards [5].

2.2.5   Hole Transporting layer (HTL):

After the generation of the electron-hole pair, the function of the HTL is to transfer the hole to their respective electrodes while blocking the electron movement. There have multiple materials that have been used as the HTL such Spiro-OMeTAD, NiO, PEDOT:PSS, CuSCN as well as organic HTL to fulfil this role [5][6].

2.2.6 Metal Contacts

Metal contacts are employed at the end of the charge transport layers. Their function is to extract and transport the charges while possessing minimum resistance and high conductivity. The selection base of the material depends upon the HOMO and LUMO levels of the layers against which they have to perform their function. Some of the materials that are used for the metal contact include Ag, Au, Cu, Al [7].

2.3 Working Principle

Upon the exposure to light to the deliverance of the charge to the load, the process involves multiple steps. The process of these steps is explained below.

2.3.1 Light Absorption

The light absorption is the responsibility of the Perovskite material in the cell. After the light is absorbed by the layer, the electrons are excited by the energy which they receive from the photons of the incident light, and they jump from the lower energy level V.B to the higher energy level C.B. The process of the absorption and excitation is shown in Figure 2.3
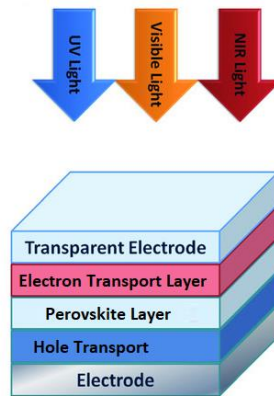
Figure 2.3: Light Absorption by Perovskite Solar Cell in n-i-p configuration

2.3.2 Excitation and Diffusion

After the light is absorbed, the electron-hole pair namely the exciton is generated. Although the exciton diffuses in the material and the electron is excited into the higher energy state but still there exists a binding energy between these two. The exciton formed depend upon the diffusion length of the material, absorption co-efficient as well as the lifetime of the carriers. If the material has shorter diffusion length and higher absorption coefficient, then a greater number of excitons will be delivered. Also, to overcome their binding energies, they must be provided with alternative interfaces which not only separates them but also deliver them efficiently to the outer circuit.

2.3.3   Charge Separation

After the light is absorbed, excitons are generated and are quickly needed to be separated. To do so we have to provide them with the alternative interfaces with suitable energy alignment [8]. But the process must be done before both carriers are attracted towards each other resulting in loss of efficiency of the cell resulting in their recombination. Recombination is regarded as one of the main reasons that have led to the decrease in the efficiency of the solar cell [9].

2.3.4   Charge Extraction

After the separation of charges, the next step is the injection of those charges to their respective charge carrier layers. The electron are transferred to LUMO of the perovskite to the LUMO of the ETL while hole are transferred to the HOMO of the perovskite to the LUMO of the HTL [8].
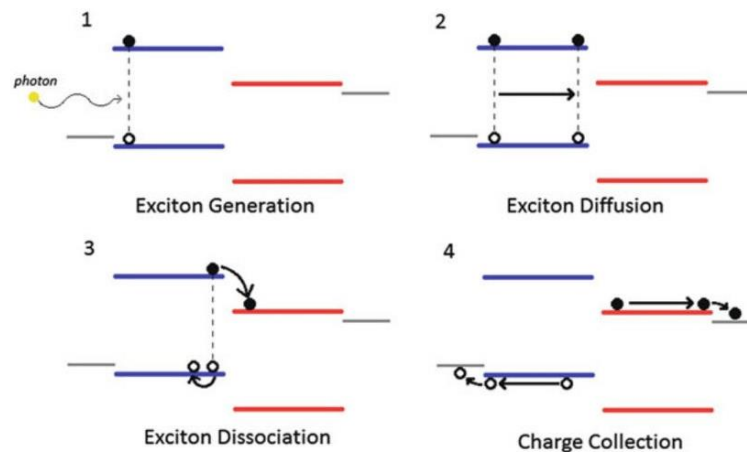
Figure 2.4: Process from Charge Generation to Collection
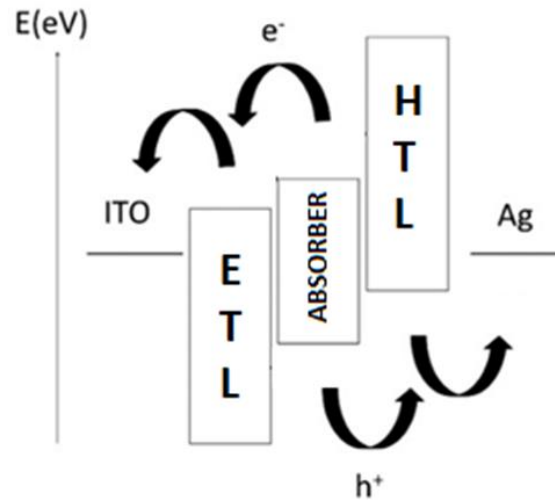
Figure 2.5: Charge Generation Process in perovskite Solar Cell

2.4 Electron Transport Layer

ETL is responsible for the transfer of electrons from absorber layer to the TCO. Mostly n-type semiconductors are recommended for their role. There are several criteria's that should be fulfilled by good ETL such as it must have low cost, can be easily fabricated, ability to block the counter carriers, high optical transmittance, high electron mobility, good band alignment and must be compatible with the absorber layer and adjacent contact [10].

There are a number of different materials that have been used as ETL. From the family of metal oxides, materials like Zn_2SO_4 [11], In_2O_3 [12], WO_3 [13], TiO_2 [5], CdS [14], CdSe [15], ZnO [16], Nb_2O_5 [17], SnO_2 [10] while SnO_2 and TiO_2 are being the widely used ones. From transitional metal dichalcogenides (TMD) potential of materials like MoS2 [18], [19] and WS_2 [20] have recently explored to be used as ETL in PSC. While from the organic family, the mostly widely used materials include C_{60} [21], C_{70} [22] and PCBM [23]. These materials have been used as either individual layers, as bi-layers or in the form of composites material for the preparation of the ETL. Their use depends upon a number of variables varying from their different properties that they offer to the architecture in which they are used.

2.4.1 Problems associated with the use of conventional ETL in PSC

TiO_2 is the most conventionally used ETL in PSC as it has low cost, well band alignment, good stability. However, TiO_2 despite being one of the most being used N-type layer has been notorious for its high temperature preparation, high defect density and long preparation time in order to achieve high carrier mobility. It has low charge carrier mobility (0.1–1 cm^2/V.s) as compared to Perovskite Material (20–30 cm^2/V.s). They suffer from rapid degeneration under UV radiation exposure [11], [24].

CdS has been one of the materials that can be prepared at low temperature from a variety of methods including low-temperature RF sputtering method, solution-processable method, chemical bath deposition method [25]. This made them suitable for both flexible applications along with its use in inverted architecture. A decent efficiency of 14.68% has been achieved with the use of CdS as ETL and EIS studies have shown that the use of CdS has caused reduction in the series resistance [26] .However, for the devices using CdS as the ETL the sulphide can cause the losses in the current. This was found because of the low band gap of the CdS film which became the reason of the parasitic absorption. While in case of CdSe the high toxicity of Cadmium was the main problem making the handling of the cadmium liquid waste difficult as they were containing solutions [10].

Similarly, ZnO is another ETL candidate that is easily available and can be easily prepared. It possesses higher electron mobility multiple times larger than the TiO_2 and have energy levels quite similar to TiO_2 and can also be processed in both compact planar and mesoporous structure. However, it suffers from the degradation problem due to the generation of vacancies of hydroxide and oxygen along with solvent residual leftover which results in deprotonation thus limiting its use as ETL [10].

Beside the inorganic ETL some organic ETL such as PCBM, Fullerene C_{60} and its derivatives, and their derivatives are also used in inverted configuration on PSC. PCBM is one of the electron acceptors that has been widely used in the organic PV. They possessed the advantage of being easily prepared via solution processing

techniques at lower temperature and are known to either shrink or eliminate hysteresis completely while exhibiting significant good performance. However, in comparison to its counterparts, while PCBM shows good solubility as compared to C_{60} and C_{70}, it's much more expressive. In addition to this, their photo-stability along with environmental and thermal were not impressive in long trends resulting in the degradation of cells [10].

2.5　Tin Oxide (SnO₂)

Tin oxide (SnO_2) is a wide-bandgap semiconductor with a high electrical conductivity and a high refractive index, making it useful in the production of transparent conductive coatings, ceramics, and electronic devices such as sensors and transistors.

It is a widely used material in the production of solar cells, particularly in thin-film solar cells. These solar cells are made by depositing a thin layer of SnO_2 on a substrate, such as glass or plastic. The SnO_2 layer acts as the light-absorbing layer, also known as the active layer, in the solar cell. The thin film of SnO_2 is usually combined with other materials to create a p-n junction that generates electricity when exposed to sunlight.

One of the advantages of using SnO_2 in solar cells is its high transparency, which allows it to act as a window layer in solar thus. This can be achieved even by utilizing a very thin layer of material, reducing the amount of material required for the solar cell. Additionally, SnO_2 is a relatively low-cost material, making it an attractive option for large-scale solar power generation.

SnO_2-based solar cells are also flexible and lightweight, which makes them suitable for use in portable and mobile applications. For its use in the solar cells, SnO_2, possess the following advantages:

i.　The SnO_2 has better electron mobility its bulk electron mobility is roughly equals to 240 cm^2/V.

ii.　It possesses a deeper conduction band resulting in faster transportation and electron extraction.

iii. Owing to its wide band gap its shows better stability and reduced photovoltaic activity.

iv. Highly optical conductive and transparent.

v. Can be fabricated via low temperature processing.

However, one of the challenges with SnO_2-based solar cells is the need for high-temperature processing, which can be expensive and energy-intensive. Therefore, to reduce the cost and overall fabrication temperature, the low temperature SnO_2 has been targeted for the fabrication of solar cells.

2.5.1 Low temperature fabrication of SnO_2

There are various methods that are used for the preparation of SnO2 which include sol-gel route, Chemical Bath Deposition (CBD), Atomic Layer Deposition (ALD) and Physical Vapor Deposition (PVD). However, regarding the low temperature preparation and the availability of equipment, the author is interested in sol get route.

2.5.2 Sol-Gel Process

The SnO_2 layer in PSCs is typically deposited using the sol-gel process. Synthesis of an integrated network begins with the formation of a colloidal solution (sol) from monomers (gel). Figure 2.6 shows the various stages of the sol-gel synthesis process. Hydrolysis and condensation of metal alkoxides are the main reactions in sol-gel chemistry. The substrate is coated with SnO_2 using a deposition method like spin coating, slot-die pyrolysis, spray pyrolysis, etc., and then subjected to thermal treatment to complete the process. The generic equations defining the process of sol-gel is defined as:

$$\text{M-OR} + H_2O \rightarrow \text{M-OH} + \text{ROH} \ (\textbf{Hydrolysis})$$
$$\text{M-OR} + \text{H O-M} \rightarrow \text{M-O-M} + \text{R-OH} \ (\textbf{Condensation})$$

Where M-OR represents the metal alkoxide, M is the metal, R is the group attached with the oxygen and M-OH is the metal hydroxide.

One common method of creating a dense SnO_2 layer is through the thermal decomposition of Sn-based salt solutions. Tin chlorides and their hydrates, such as $SnCl_2$, $SnCl_2.2H_2O$, or $SnCl_4.5H_2O$, are typically dissolved in an alcohol-based solvent to make the sol-gel precursor solution. The quality of the SnO_2 layer is determined by the annealing process, which is performed in ambient air to transform the Sn-based sol-gel into SnO_2. In most cases, it's preferable to work at temperatures below 200 degrees Celsius. While increasing the annealing temperature usually improves SnO_2's crystallinity, doing so can increase the number of oxygen defects and pinholes in the films, which is bad for the performance of the devices [27]. In addition, the wettability of the sol-gel can be improved prior to deposition with UV-ozone (UVO) treatment, and residuals can be removed following annealing.
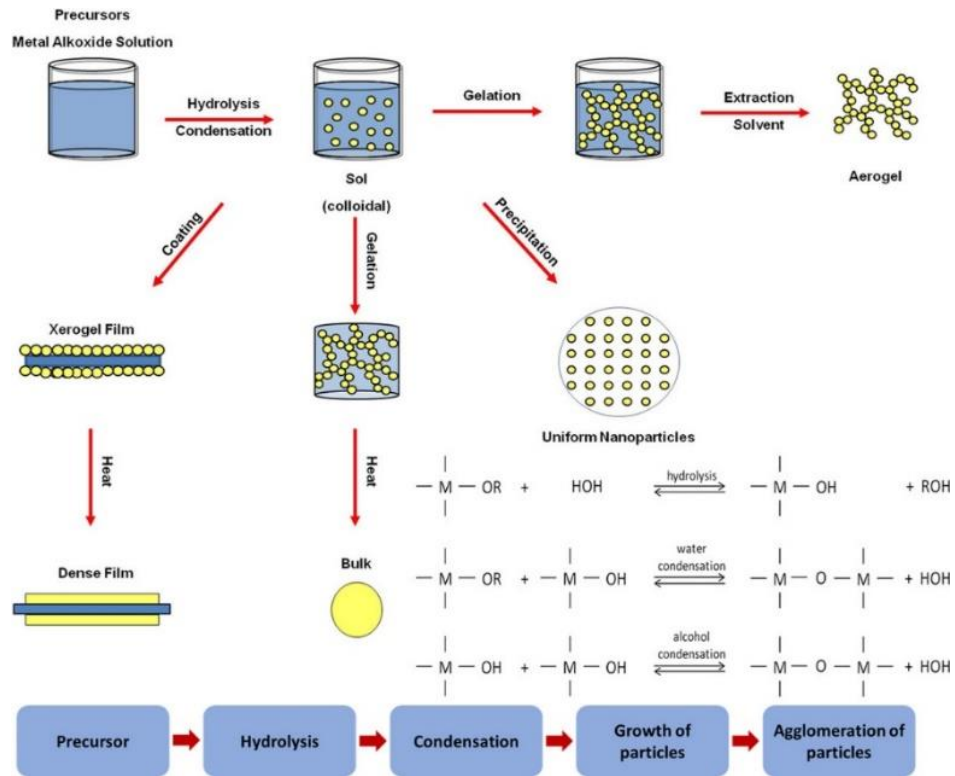
Figure 2.6: Diagram of Sol-gel route with different condition resulting on the formation of different final products including xerogels, aerogels and monomers nanoparticles [28]

SnO_2 organic sol was prepared by dissolving $SnCl_2.2H_2O$ in ethyl alcohol by Ma et al., in 2015, and then the film was coated on FTO substrates and sintered at 450 °C to achieve a PCE of 7.43% [28]. According to research by Yan et al., who

investigated the impact of annealing temperatures on $SnCl_2$-based sol-gel, PSCs containing low-temperature SnO_2 performed better than those containing high-temperature SnO_2 [29].
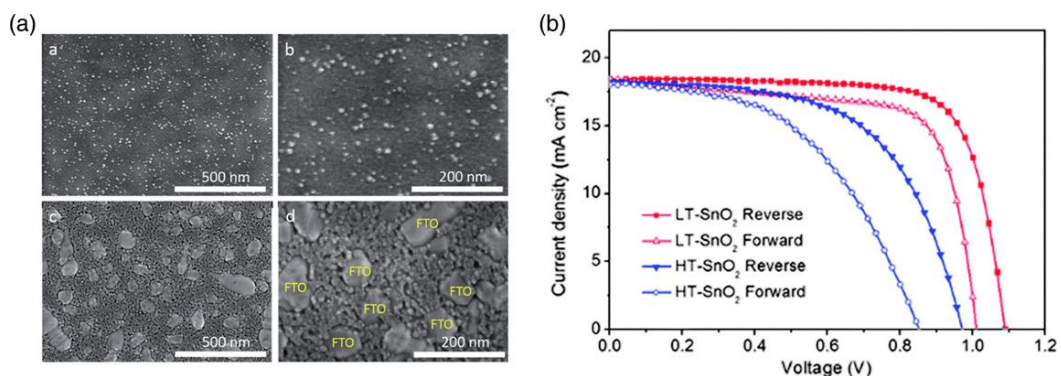
Figure 2.7: (a) Top images showing High Temperature annealed SnO2 with thickness of 40 nm and bottom images showing Low Temperature annealed layer of SnO2 with 40 nm thickness (b) IV curve of PSC prepared with low temperature and high temperature annealed SnO2 layer [26]

Figure 2.7 displays SEM images of high-temperature processed SnO_2 and low-temperature processed SnO_2 from the top down. Although high-temperature SnO_2 displays significantly improved crystallinity, the film is not compact and cannot effectively block holes, resulting in severe interface recombination and a shunting path. [27] The SnO_2 ETL was then optimized by Yan and colleagues using $SnCl_2.2H_2O$ in ethanol, leading to a respectable PCE of 17.21% [29]. It may be simpler to achieve good device performance by depositing pre-synthesized nanoparticles to form a dense and compact SnO2 layer. Making SnO2 sol-gel from hydrolysis and polymerization of Sn-salt precursors yields the nanoparticles or quantum dots of interest. Refluxing allows atmospheric oxygen and water to participate in the synthesis, which is essential for promoting Sn^{2+} oxidation and regulating hydrolysis in the Sn-salt precursors. It might be possible to get rid of the residues by washing them away [30].

SnO_2 nanocrystals were synthesized by Jen et al. [31] using a hydrothermal route. To achieve this, they added $SnCl_4.5H_2O$ and aqueous TMAH to ethanol and autoclaved the mixture at 200 °C for 12 hours. Spin coating can be used to apply the obtained sol-gel nanocrystals to an inverted structure, making them suitable for use

as an ETL. Using a configuration of FTO/NiO/MAPbI$_3$/C$_{60}$/hydrothermal SnO$_2$/Ag, the PSC was able to achieve PCE of 18.80 percent. [31] Jiu and coworkers have also done related work via a similar synthesis strategy. When SnO$_2$ nanoparticles were incorporated into PC$_{61}$BM, the electron charge transport was greatly improved, and the recombination loss was decreased, resulting in a PCE increase from 13.2% to 19.7% in an inverted structure [32].

A simple method for synthesizing SnO$_2$ nanocrystals at temperatures below 80 °C was proposed by Wang et al. [33] in 2017 (Figure 2.8). The resulting SnO$_2$ nanocrystals had a diameter of less than 5 nm, allowing for PCEs greater than 19% [33]. Quantum dot colloidal synthesis at room temperature and additive removal at low temperatures were introduced as part of a two-step synthesis procedure by Liu et al. [34]. Completely exposing the SnCl$_2$.2H$_2$O/CH$_4$N$_2$S aqueous solution to air without thermal treatment yielded fine SnO$_2$ quantum dots with a size of 3-5 nm. The PCE output of the champion cell is extremely high, at 20.32% [35].\
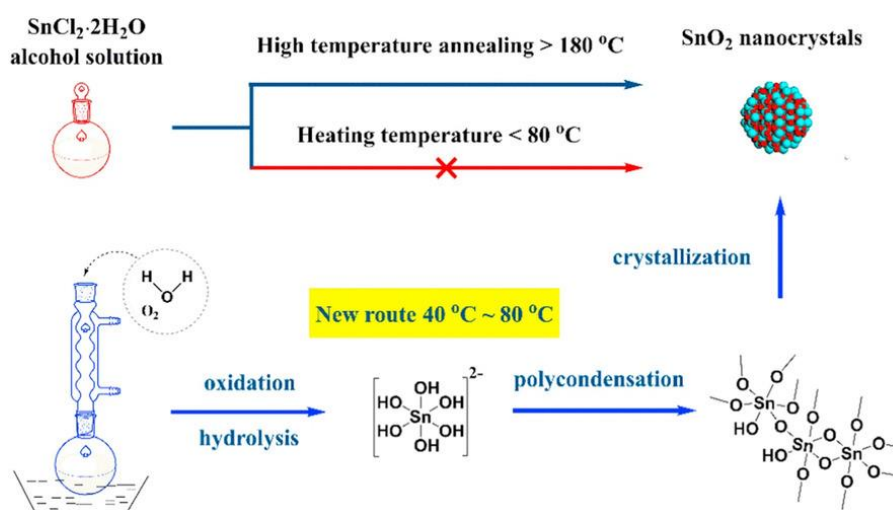
Figure 2.8: Schematic diagram for the preparation of nanocrystals of SnO$_2$ at low temperature [33]

A PCE of 19.90% was first achieved by Jiang et al. [36] in 2016, using a commercially available SnO$_2$ colloid precursor to fabricate PSC. Spin coating with a diluted SnO$_2$ nanoparticles solution and an annealing treatment at 150 °C were used to produce the final product. When using a configuration of ITO/SnO$_2$/(FAPbI$_3$)$_{0.97}$(MAPbBr$_3$)$_{0.03}$/Spiro-OMeTAD/Au, we were able to achieve

a PCE of 19.90% in our champion cell. [36] By fine-tuning the PbI$_2$ passivation layer, we were able to increase efficiency to 21.6% [36]. In 2019, Your group improved upon their result with PEAI passivation on the perovskite absorber, increasing it to 23.32% (quasi-steady state) [37]. Researchers from other groups also adopted this simple method and obtained decent results [38]. Liu et al., for instance, used EDTA to further purify SnO$_2$ nanoparticles, resulting in a certified PCE of 21.52% by Newport [39]. However, Tan et al. found that when potassium chloride (KCl) was mixed with SnO$_2$ nanoparticles, the K$^+$ and Cl$^-$ ions could passivate the ETL/perovskite interface trap centers simultaneously. They were able to increase the open-circuit voltage from 1.077 V to 1.137 V, which resulted in a PCE of 22.2% [40].

2.5.3   Modification of SnO$_2$

There are various methods that are used for the preparation of SnO$_2$. Due to the difference in these preparation techniques, there occurs difference in the properties of the same materials. Therefore, modification of SnO2 via various methods is a suitable method to improve the intrinsic defects thus improving their properties. Some of these methods include elemental doping, surface treatment, bilayer and composite layers.

2.5.3.1   Doped SnO$_2$ ETL for PSC

Doping is a process in which impurities are introduced in the intrinsic materials. By introducing these impurities, the electrical optical and electrical properties of the material are modified and are somewhat changes to achieve the desired results. In summary, doping is performed to not only form an efficient layer but also enhance the crystallinity of the layer, improves the defects while enhancing the electrical properties such as the Voc and Jsc. The dopants have proved not only to improve the morphology but also reduces the charge traps and hysteresis which is one of the many problems currently faced by the PSC. Besides this, it also provides excellent stability, better band alignment and improved charge mobility and conductivity. In case of PSC, the balance of charge transport between ETL and HTL is one of the crucial parameters that affects the overall performance of the

device. Therefore, doping seems to be an effective strategy to improve the properties of ETL but also the properties of the interface that exist between ETL and Perovskite. Multiple dopants have been reported to improve the performance of the SnO$_2$ based ETL inn comparison to their intrinsic counterpart.

Bahadura et. al. has doped the SnO$_2$ ETL with Molybdenum in the ambient condition. With the 1% optimum amount of dopant added, the ETL fabricated resulted in the tightly packed structure along with the upshift of Fermi level [24]. Park et. al doped SnO$_2$ with Lithium. The addition of Lithium resulted in the increase in the grain boundaries higher as compared to the un-doped layer which reduces the trap states of the layer. Also, there was reduction in recombination and increase in mobility [41]. Niobium doped in the SnO$_2$ layer resulted in a remarkable efficiency of the 20.07%. It also increased the short circuit current density of the device and reduced the recombinations [42].

It is shown that Gallium doping by Maa et al has significantly reduced the hysteresis index factor. The doping has also shifted the fermi level upwards with higher electron mobility and optimized band gap alignment [43]. The addition of Lanthanum to the SnO$_2$ by Xua et al., [44] has shown to improve the surface morphology of the film along with the aggregation of the crystal as shown in in the . Without affecting the morphology of the film, the dopant shifted the conduction band minima upward and reduced the recombination along with the increase in charge injection rate. The Sb doped SnO$_2$ layer resulted in the upward shift of energy level due to improved energy level alignment and also improved the electrical conductivity by enhancing the carrier concentration and increasing the recombination lifetime of the electron [44].

In addition to being singly doped by the elements, the Quantum Dot ETL of SnO$_2$ based material has been co doped from the Zr/F. The doping of the Zr has caused the uplift in the energy levels of the ETL to make it match better with the Perovskite layer. Also, the addition of the F has imparted extra electrons to the layer resulting in the presence of extra charge carriers and increased conductivity. Also, since the atomic radii of the both the element is close to the Sn and O, so as a result

the dopant has easily incorporated into the layer resulting in no substitutional defects [45].
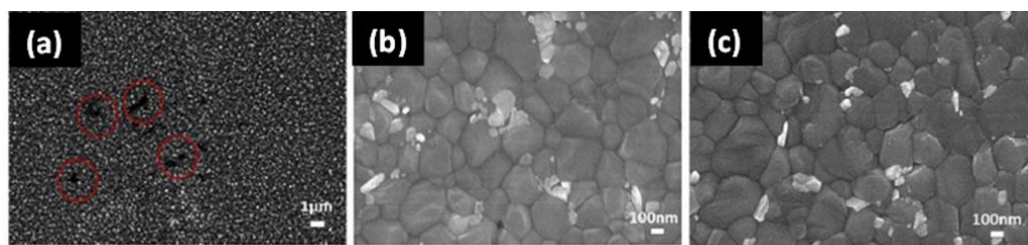
Figure 2.9: Improved Morphology due to doping of lithium [44]

Similar to addition of the lanthanum, the addition Polyethyleneimine (PEIE) also shifted the C.B. upwards. Due to the presence of the amine group, they have the ability of donating electron hence acting as n-type hence suitable for the role of ETL. It has also reduced the work function of the ITO substrate and has improved the surface roughness of the layer with better energy level alignment while achieving an efficiency of 20.61% [46].

Dong et al., adopts a simple method by of doping SnO_2 by Na^+ Cl^- simultaneously. This resulted in the reduction of defects at the interface of SnO_2 and Perovskite along with the reduction at grain boundaries. Furthermore, a decent the PCE was also achieved increasing from 16.66% to 18.56% [47]. Beside this, Graphite carbon nitride (GCN) was also doped which resulted in the increased efficiency of PSC over 22% [48].

Another metallic dopant that has gained a very decent PCE is Zr. The Zr doped NP of SnO_2 were able to bestow PSC with excellent conductivity by improving its charge extracting capability. Besides this it also suppressed the current leakage between the ETL and perovskite layer by reducing the interfacial resistance between those two layers. The device prepared also showed suppressed hysteresis [49]. Similarly, Song et. al [50] prepared the nanocrystals of the Y^{3+} doped SnO_2 with the help of solvothermal method and later the solution was spin coated on the substrate. The addition of dopant allowed the enhancement of the electrical parameters along with obtaining an upstanding PCE of 20.71% with decent band alignment and low hysteresis as compared to its undoped counterpart. Yttrium has also been used for

the fabrication of flexible inverted structured PSC to improve the properties of solution processed SnO_2. The addition of Y along with the functionalization of nano particles of SnO_2 with acetate on top of perovskite via doctor blading resulted in the improved device performance due to decrement in the series resistance. As a result of this the Voc and FF was improved leading to improved device performance of 16.5% PCE [51].

Table 2.1: Parameters of PSC based on the addition of different dopant.

Dopant	V_{oc} (V)	J_{sc} (mA cm^{-2})	FF (%)	PCE (%)	Ref.
Mo^{+5}	0.972	15.20	72.01	10.52	[24]
Li^{+1}	1.106	23.27	78.05	18.20	[41]
Ga^{+3}	1.068	23.90	74.81	18.18	[43]
Zr	1.08	25.30	73.53	19.54	[49]
Sb^{+5}	1.06	22.6	71.55	17.2	[44]
Y^{3+}	1.13	23.56	79.03	20.71	[50]
Nb^{+5}	1.10	23.21	76.43	20.07	[42]
La	1.09	21.77	69.21	17.08	[44]
PEIE	1.14	23.83	72.18	20.61	[52]
NaCl	1.11	22.2	75.37	18.56	[47]
GCN	1.1163	23.308	79.18	21.24	[48]
Y	1.08	22.40	68.4	16.5	[51]
Cu	1.108	79.02	24.21	21.35	[53]
Gd	1.143	23.80	82	22.40	[54]
$CuCl_2$	1.13	23.69	76.19	20.31	[55]

The Cu doping also affected the band position of SnO_2 and increased the conduction band of the SnO_2. As a result of this doping the conductivity of the layer was increased. The doping also improved crystallinity and increased the grain size of perovskite absorber layer. The cell achieved a decent efficiency of 21.35% along with improved stability under light or thermal conditions [52]. Rare earth metal

Gadolinium[53] was doped in SnO_2. The addition reduced the traps at the interface leading to reduced recombination. The addition also resulted in a better energy level with the perovskite absorber layer along with obtaining a decent device efficiency of 22.4%. the addition of anhydrous copper chloride ($CuCl_2$), improved the conductivity and hydrophobicity of ETL along with suitable energy level alignment. As a result of this the stability and PCE of the PSC were increased with device able to retain 89.3% of efficiency for 16 days [54].

2.5.4 Metal Oxide Composite

Since in planar PSC in which SnO_2 is used as ETL, they are mostly prepared by adopting low temperature synthesis routes therefore a very thin thickness of film is obtained. This not only results in the non-homogenous deposition of the film but also leads to formation of pin holes and defects in the film. Therefore, to improve these defects and overcome these challenges, SnO_2 has been combined with other metal oxides layer to improve the photovoltaic performance of cells. It should be noted that formation of metal oxide composite is different from the mechanism of doping since in doping the additional impurity is introduced while in metal oxide composites a second layer of metal oxide is deposited on the top of the first layer. This not only covers the first layer resulting in the coverage of pin holes and of the first layer but with the proper energy alignments charge extraction can be carried out effectively. Different metal oxides are used with SnO_2 to form metal oxide composites including MgO, ZnO and TiO_2 in PSC.

In 2018, Zhong et al. [52] created a bilayer ETL by stacking SnO_2 on top of TiO_2. It was hypothesized that a stacked n-layer, consisting of SnO_2 on top of TiO_2, would fully inhibit hole transport to TiO_2, thereby eliminating the defects generated at the TiO_2/perovskite interface. The PCE was raised from 17.35% to 18.03% using the stacked bilayer ETL, which is an improvement over the SnO_2 PSC. An increase in J_{sc} due to better perovskite quality was credited for the boost. Instead, a SnO_2/TiO_2 bilayer was formed by spin coating TiO_2 nanoparticles onto SnO_2 ETL, as shown by Cheng and colleagues. Cascade-aligned energy levels formed by the proper stacking of bilayers could reduce the significant energy shift. Also, the perovskite that was

grown on the SnO_2/TiO_2 bilayer crystallized more successfully, with larger, more dense crystals and fewer pinholes. The J_{sc}, V_{oc}, and FF have all been improved at the same time as a result of the material's superior defect-passivation ability. Overall effectiveness increased from 18.09% to 20.50% as a result [53].

For a $MAPbI_3$-based device, Chen and colleagues developed a ZnO/ SnO_2 double layer. This higher Voc was traced to the fact that more electrons were being injected into SnO_2 and transported to ZnO. Although the Jsc has decreased slightly, the PCE has been raised from 18.0% to 19.1% by pairing ETLs with a higher Fermi level EF and conduction band energy ECBM [54]. $ITO/ZnO/SnO_2/perovskite/Spiro-OMeTAD/Au$ was formed using a similar strategy by Ye et al.[55]. Electrons can flow freely from the SnO_2 layer to the ITO electrode thanks to the ohmic contact formed by the bending of the energy band edge caused by the ZnO modification in the SnO_2 ETL. However, compared to a pure SnO_2 film, the ZnO/SnO_2 hybrid showed improved electrical conductivity. Increased from 18.76% to 20.45%, the PCE of PSCs with a bilayer ETL of 10 nm ZnO and 20 nm SnO_2 showed significant improvement. The increased crystallization property of perovskite and enhanced charge transport and extraction at the interface were made possible by the addition of a ZnO layer, which not only decreased the surface roughness and work function of ITO but also improved the electrical properties of the SnO_2 ETL. [56], [57]

By adding a thin layer of MgO to the SnO_2 ETL, Brown et al. were able to increase the PCE by 20%. Higher rectification ratios were achieved thanks to the MgO layer, and the devices were also more stable and had less hysteresis at low light levels. The highest PCE they were able to achieve was 19%, and they settled on an 18.1% average [58]. Besides the formation of bilayers, different metal oxide can also be mixed to form composites with SnO_2. Since different meta oxides have different work functions, therefore by mixing different types of materials, their band energy level and work function can be tuned thus facilitating the charge extraction properties of ETL. In 2016, Miyasaka and coworker formed a nanocomposite planar ETL by different SnO_2 and ZnO nanoparticles in different ratio's (1:2 wt%) respectively. The resulting conduction band edge from this composite was -4.25 eV

lying in the range of -4.2 eV to -4.5 eV in SnO_2. As a result of this tailoring of band level a PCE of 14.5% was achieved [59].

Besides the widely explored MO composites, composite SnO_2 has also been explored with the stannate particularly Barium Stannate ($BaSnO_3$). The formation of composite resulted in stable and efficient PSC. Beside this, the addition of $BaSnO_3$ in combination with SnO_2 lead to enhance the stability of the device particularly in UV region. The composite not only allowed to improve the PCE of the device but also allowed the device to retain its performance for longer period of time [65]. The formation of composite with the polymer has also been explored. The polymer P123 which is a non-ionic surfactant was used to suppress the agglomeration of particles leading to re compact and uniform film. The device exhibited an improved champion efficiency of 17.44% while retaining 85% of the efficiency for over 1000 hours [66].

The F-doped TiO_x was used to form composite with SnO_2. The F-doped TiO_x not only filled the cracks but also act as intermediate level allowing the for better charge transport due to availability of channels, passivates the oxygen vacancies effectively, optimized the energy levels and enhanced the electron mobility significantly leading to reduce charge transport. Due to the addition of composite, the cell achieved a decent efficiency of 22.70% along with good operational stability [67]. To further enhance the light transmission from the SnO_2 and ITO along with enhancing the stability of PSC device D-Arg was introduced. The composite allowed the device to retain more than 84% of the performance after 720h while increasing the transparency window of the electrode up to 94% [68]. To improve the fill factor of the device, WO_3 was added with SnO2 alkaline colloidal solution. The formation of nanocomposite resulted in the reduction in S and oxygen vacancies sites as a result of healing of hydroxyl group. The device delivered a staggering fill factor of 85.8% along with a decent efficiency of 23.6%.

To facilitate the transport of electrons, Yang et al. developed a composite of SnO_2 and TiO_2 called a gradient heterojunction (GHJ). Electrons can be efficiently extracted from the slow mobility TiO_2 network to the high mobility SnO_2 network

thanks to the GHJ formed at the boundaries of the interconnected SnO_2 and TiO_2 frameworks. Using the TiO_2/SnO_2 composite ETL, they were able to get a PCE of 18.08% [60].

Table 2.2: Parameters of PSC from the formation of different composites

Composite	V_{oc} (V)	J_{sc} (mA cm^{-2})	FF(%)	PCE (%)	Ref.
SnO_2/TiO_2	1.085	22.30	75.4	18.03	[56]
SnO_2/TiO_2	1.10	24.2	78.7	20.5	[57]
SnO_2/Zr	1.08	25.30	75.6	19.54	[58]
SnO_2/ZnO	1.15	21.74	76.9	19.1	[59]
SnO_2/ZnO	1.16	23.07	78.8	20.45	[60], [61]
SnO_2/ZnO	1.10	22.88	75.3	19.52	[57]
SnO_2/MgO	1.12	21.26	71.6	17.92	[62]
SnO_2/TiO_2	1.05	18.8	69.9	13.7	[63]
SnO_2/TiO_2	1.012	18.08	72.5	18.08	[64]
$SnO_2/BaSnO3$	1.02	22.81	66.35	15.54	[65]
$SnO_2/P123$	1.162	21.69	77.1	17.44	[66]
$F-TiOx/SnO_2$	1.13	24.57	81.66	22.70	[67]
$SnO_2/D-Arg$	1.161	24.51	76.07	21.74	[68]
SnO_2/WO_3	1.147	23.98	85.8	23.6	[69]

2.6   Transitional Metal Dichalcogenide (TMD's)

Transition metals belong to the category of the periodic table that has incomplete d-subshell (in d-subshell there maximum 10 number of electrons can be compensated) while chalcogen refers to the chemical compound that has at least one chalcogen anion (meaning it has negative charge on it).TMDs, in particular, present

the MX_2 structure, where M is a transition metal of groups 4–10 (typically Mo, Nb, W, Ni, V, or Re) and X is a <u>chalcogen</u> (typically Se, Te or S) acting as semiconductors (MoS2, WS_2), metals or semi-metals (TaS_2, NbS_2).

TMDs are characterized by strong covalent bonds providing the stability of 2D crystals, as well as weak van-der-Waals (40–70 meV) forces between the planes. Such forces are prone to be broken, facilitating controllable liquid exfoliation in a range of common solvents. In particular, the heterostructures of semiconducting two-dimensional (2D) transition metal dichalcogenides (TMDs) are interesting due to the quantum confinement effect, extended solar light absorption, and tunable optoelectronic properties.
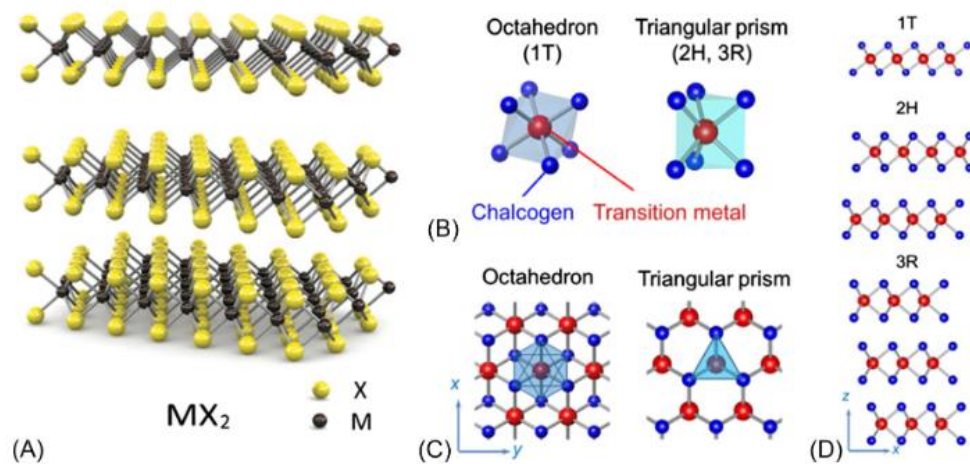
Figure 2.10: (A) 3D representation of TMD's (B) Archetypal coordination in TMD's shown by octahedron and triangular prism representing 1T and 2H,3R structure respectively (C)Top view of the structure represented by octahedron & Triangular prism (D) Side view of 1T, 2H and 3R. [61]

2.7 MoS_2

MoS_2 belongs to the family of the TMD. Molybdenum belongs to the transitional metals while sulfur belongs to the chalcogenide family. They are a new family of the 2D nanosheets that has the general formula of the MX_2 where M is the transition metal and X is the chalcogenide. It is one of the materials that have used widely in the role of both ETL and HTL respectively.

In MoS$_2$, sulfur being the chalcogenide possess the oxidation state of -2 while Mo being the transitional metal has the oxidation states varying between +2 to +6 but in this case, it kept the +4-oxidation state. Together the unit they form is X-M-X and the lone pairs terminate the surface (meaning there are no dangling bong on the surface). They usually form the structure 1-trigonal, 2-hexagonal, and 3-rhombohedral with the digits representing the no. of units in the structure [61]. The properties of MoS$_2$ vary to a great length based on their thickness making them useful to a wide range of application.

Owing to its high carrier mobility, large bandgap and compatibility to be deposited with CVD, MoS$_2$ has shown its potential to be PSC serving its dual role in charge transport layers. Through the change in chemical composition, doping and surface functionalization, the work function of MoS$_2$ can be tailored in the range of 3.5 eV-4.8 eV depending upon the approach.

2.7.1 MoS$_2$ based Electron Transport Layer

MoS$_2$ ETL has been used in PSC for the first time by Singh et al. in 2019 [19], when they microwave-irradiated a glass/FTO substrate to deposit the material. The physical parameters were studied, and results were compared to those from the most advanced ETLs on the market, TiO$_2$ and SnO$_2$. Glass/FTO/MoS$_2$/perovskite/Spiro-OMeTAD/Au cells were used to fabricate the PSC device, which demonstrated a device efficiency of 13.1%, which was much closer to the efficiency of the commonly used ETLs TiO$_2$ and SnO$_2$.
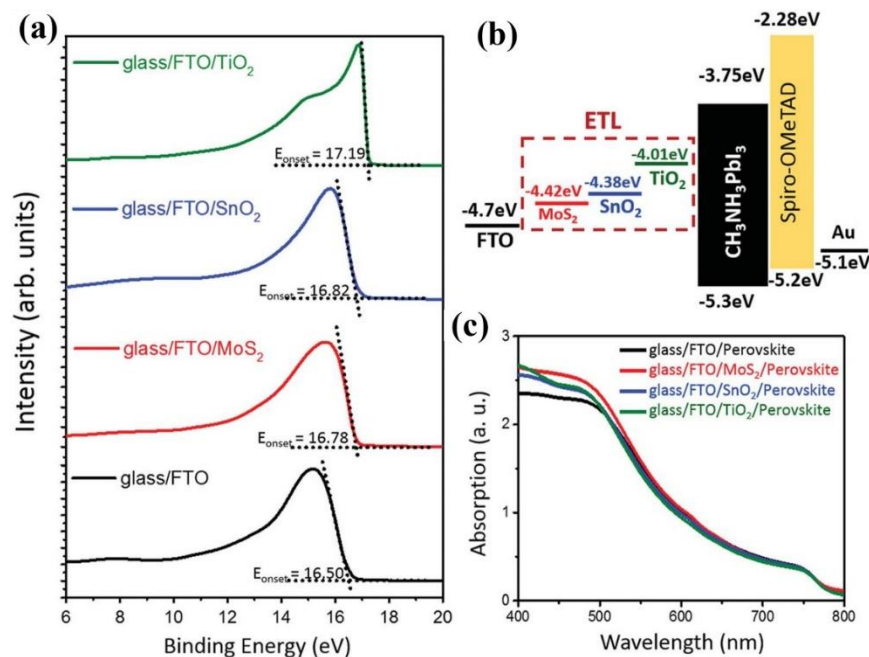
Figure 2.11: (a) Ultraviolet photoelectron spectroscopy (UPS) used for the calculation of work function of metal oxide (b)energy level diagrams of complete PSC device (c) UV-Visible spectroscopy Absorbance spectra of Perovskite layer with different ETL [19]

UV photoelectron spectroscopy (UPS) was used to determine the work functions of various ETLs, yielding values as follows Figure 2.11(a)): FTO (4.7eV), MoS_2 (4.42), SnO_2 (4.3eV), TiO_2 (4.01eV). Energy-level diagrams for each PSC layer were drawn according to the data obtained from the UPS, as shown in Figure 2.11 (b). In addition, the UV visible absorption spectra of the perovskite light-absorbing layer deposited on glass/FTO, glass/FTO/TiO_2, glass/FTO/SnO_2, and glass/FTO/MoS_2 device configurations are displayed in Figure 2.11 (c). The glass/FTO/perovskite structure has demonstrated lower absorbance in the 400-500 nm range, whereas the glass/FTO/MoS_2/perovskite film demonstrated relatively higher absorbance in the 420-600 nm region, leading to improved light diffusion.

Electrospray-deposited MoS_2 nanosheets have been used as an ETL in PSC, allowing Mahmood et al. to achieve a 16.17% champion PCE while also improving stability and lowering hysteresis. MoS_2 allowed for the development of solution-processable, low-cost, and stable PSCs with PCEs on par with commonly used ETLs (TiO_2 and SnO_2) [62]. Ultrathin layers of MoS_2 were synthesized using ultrasonic

35

spray pyrolysis. It was seen that the properties of the cell was greatly affected by the homogeneity and the quality of the layer grown on the substrate. The temperature range used for the synthesis of the MoS$_2$ nanosheets varied between 180 ºC and 250 ºC. It was found that the optimum temperature for the MoS$_2$ was 200 ºC where the layer deposited were not only homogeneous but reduction in the formation of Nano particles was also seen which increases in the increasing temperature as can be seen in the Figure 2.12. In addition to this the formation of nanoparticles also resulted in the reduction of the device performance. The thickness achieved at this temperature was 5 layers and the champion efficiency achieved was 3.36% with the device showing stability up to 80sec under 1 sun [18].
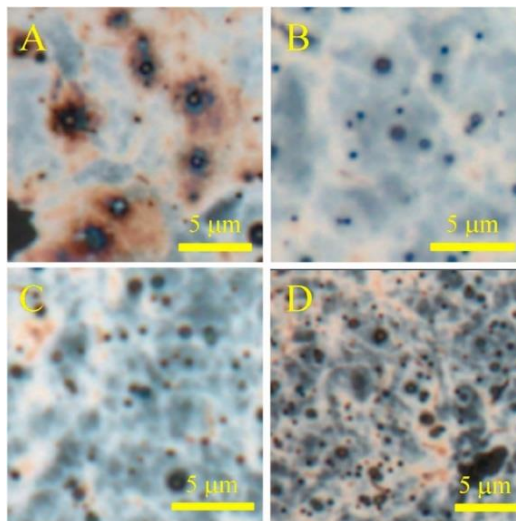
Figure 2.12: Nano sheets of MoS$_2$ prepared at different temperature (a) 180 ºC (b) 200 ºC (c) 220 ºC (d) 250 ºC. The MoS$_2$ film is represented by bluish color while the nanoparticles are represented by black color [18]

Despite the remarkable properties exhibited by MoS$_2$ and SnO$_2$, the investigation and application of the SnO$_2$-MoS$_2$ composite have thus far been constrained to its role in supercapacitors [63], gas sensors [64], energy storage [65], and photocatalytic applications [66]. Notably, the exploration of its potential as a Nano flake-based electron extractor remains unexplored (to the best of our knowledge). Consequently, this study presents a novel approach where Pristine Nano Flakes of MoS$_2$ are added in SnO$_2$, forming a nano-composite layer for

examining its impact on optical, electrical, and morphological properties along with its application of solar cell.

Summary

This chapter summarizes the basics of perovskite solar cell, the description of the components that are involved in the fabrication of PSC, its working principle and the process that occur in the PSC responsible for the generation of current from light. Then the role of ETL is discussed in PSC along with the properties they should possess to play their effective role for charge extraction. This is followed by the discussion of problems that are associated with the conventionally used ETL.

After that the role of SnO_2 in PSC is discussed, what are their properties that make them superior to other metal oxide ETL's. Then the sol-gel route is discussed which is used for the low temperature synthesis of SnO_2. This is followed by a comprehensive discussion on the modification of SnO_2 prepared by low temperature synthesis route via doping and formation of nanocomposite layers. Finally, TMD's are discussed along with the properties that make them suitable candidates to play their dual role for the charge extraction in PSC. Furthermore, the role of MoS_2 as ETL is discussed based on the properties like thickness, temperature and the method used for its synthesis.

References

[1]   J. Chen *et al.*, "Graphitic carbon nitride doped SnO2 enabling efficient perovskite solar cells with PCEs exceeding 22%," *Journal of Materials Chemistry A*, vol. 8, no. 5. pp. 2644–2653, 2020. doi: 10.1039/c9ta11344d.

[2]   Q. Liu *et al.*, "Effect of tantalum doping on SnO2 electron transport layer via low temperature process for perovskite solar cells," *Appl Phys Lett*, vol. 115, no. 14, p. 143903, Oct. 2019, doi: 10.1063/1.5118679.

[3]   NREL, "Best Research-Cell Efficiency Chart | Photovoltaic Research | NREL." https://www.nrel.gov/pv/cell-efficiency.html (accessed Jan. 26, 2022).

[4]   A. Kojima, K. Teshima, Y. Shirai, and T. Miyasaka, "Organometal halide perovskites as visible-light sensitizers for photovoltaic cells," *J Am Chem Soc*, vol. 131, no. 17, pp. 6050–6051, May 2009, doi: 10.1021/JA809598R/SUPPL_FILE/JA809598R_SI_001.PDF.

[5]   J. Wang *et al.*, "Functional Metal Oxides in Perovskite Solar Cells," *ChemPhysChem*, vol. 20, no. 20, pp. 2580–2586, Oct. 2019, doi: 10.1002/CPHC.201900447.

[6]   S. Li, Y. L. Cao, W. H. Li, and Z. S. Bo, "A brief review of hole transporting materials commonly used in perovskite solar cells," *Rare Metals*, vol. 40, no. 10, pp. 2712–2729, Oct. 2021, doi: 10.1007/S12598-020-01691-Z/TABLES/4.

[7]   S. Kohnehpoushi, P. Nazari, B. A. Nejand, and M. Eskandari, "MoS2: a two-dimensional hole-transporting material for high-efficiency, low-cost perovskite solar cells," *Nanotechnology*, vol. 29, no. 20, p. 205201, Mar. 2018, doi: 10.1088/1361-6528/AAB1D4.

[8]   I. Mora-Seró, "How Do Perovskite Solar Cells Work?," *Joule*, vol. 2, no. 4, pp. 585–587, Apr. 2018, doi: 10.1016/J.JOULE.2018.03.020.

[9]   "Types of Recombination | PVEducation." https://www.pveducation.org/pvcdrom/pn-junctions/types-of-recombination (accessed Jan. 26, 2022).

[10]   Q. Jiang, X. Zhang, and J. You, "SnO2: A Wonderful Electron Transport Layer for Perovskite Solar Cells," *Small*. 2018. doi: 10.1002/smll.201801154.

[11]   X. Liu, C. C. Chueh, Z. Zhu, S. B. Jo, Y. Sun, and A. K. Y. Jen, "Highly crystalline Zn2SnO4 nanoparticles as efficient electron-transporting layers toward stable inverted and flexible conventional perovskite solar cells," *J Mater Chem A Mater*, vol. 4, no. 40, pp. 15294–15301, Oct. 2016, doi: 10.1039/C6TA05745D.

[12]   M. Qin *et al.*, "Perovskite Solar Cells Based on Low-Temperature Processed Indium Oxide Electron Selective Layers," *ACS Appl Mater Interfaces*, vol. 8, no. 13, pp. 8460–8466, Apr. 2016, doi: 10.1021/ACSAMI.5B12849/SUPPL_FILE/AM5B12849_SI_001.PDF.

[13]   K. Wang *et al.*, "Low-temperature and solution-processed amorphous WOX as electron-selective layer for perovskite solar cells," *Journal of Physical Chemistry Letters*, vol. 6, no. 5, pp. 755–759, Mar. 2015, doi: 10.1021/ACS.JPCLETT.5B00010/SUPPL_FILE/JZ5B00010_SI_001.PDF.

[14]   C. D. Wessendorf, J. Hanisch, D. Müller, and E. Ahlswede, "CdS as Electron Transport Layer for Low-Hysteresis Perovskite Solar Cells," *Solar RRL*, vol. 2, no. 5, p. 1800056, May 2018, doi: 10.1002/SOLR.201800056.

[15]   X. Zeng *et al.*, "Performance improvement of perovskite solar cells by employing a CdSe quantum dot/PCBM composite as an electron transport layer," *J Mater Chem A Mater*, vol. 5, no. 33, pp. 17499–17505, Aug. 2017, doi: 10.1039/C7TA00203C.

[16]   F. Yang, D. W. Kang, and Y. S. Kim, "Improved interface of ZnO/CH3NH3PbI3 by a dynamic spin-coating process for efficient perovskite solar cells," *RSC Adv*, vol. 7, no. 31, pp. 19030–19038, Mar. 2017, doi: 10.1039/C7RA01869J.

[17]   J. Feng *et al.*, "E-beam evaporated Nb2O5 as an effective electron transport layer for large flexible perovskite solar cells," *Nano Energy*, vol. 36, pp. 1–8, Jun. 2017, doi: 10.1016/J.NANOEN.2017.04.010.

[18]   N. A. Abd Malek *et al.*, "Ultra-thin MoS2 nanosheet for electron transport layer of perovskite solar cells," *Opt Mater (Amst)*, vol. 104, p. 109933, Jun. 2020, doi: 10.1016/J.OPTMAT.2020.109933.

[19]   R. Singh *et al.*, "Perovskite solar cells with an MoS2 electron transport layer," *J Mater Chem A Mater*, vol. 7, no. 12, pp. 7151–7158, Mar. 2019, doi: 10.1039/C8TA12254G.

[20]   N. A. A. Malek *et al.*, "Enhanced Charge Transfer in Atom-Thick 2H–WS2 Nanosheets' Electron Transport Layers of Perovskite Solar Cells," *Solar RRL*, vol. 4, no. 10, Oct. 2020, doi: 10.1002/SOLR.202000260.

[21]   C. Bi, Y. Yuan, Y. Fang, and J. Huang, "Low-temperature fabrication of efficient wide-bandgap organolead trihalide perovskite solar cells," *Adv Energy Mater*, vol. 5, no. 6, Mar. 2015, doi: 10.1002/AENM.201401616.

[22]   J. Pascual *et al.*, "Electron Transport Layer-Free Solar Cells Based on Perovskite–Fullerene Blend Films with Enhanced Performance and Stability," *ChemSusChem*, vol. 9, no. 18, pp. 2679–2685, Sep. 2016, doi: 10.1002/CSSC.201600940.

[23]   J. Seo *et al.*, "Benefits of very thin PCBM and LiF layers for solution-processed p–i–n perovskite solar cells," *Energy Environ Sci*, vol. 7, no. 8, pp. 2642–2646, Jul. 2014, doi: 10.1039/C4EE01216J.

[24]   J. Bahadur, A. H. Ghahremani, B. Martin, T. Druffel, M. K. Sunkara, and K. Pal, "Solution processed Mo doped SnO2 as an effective ETL in the fabrication of low temperature planer perovskite solar cell under ambient conditions," *Org Electron*, 2019, doi: 10.1016/j.orgel.2019.01.027.

[25]   A. Raj, M. Kumar, and A. Anshul, "Recent advancement in inorganic-organic electron transport layers in perovskite solar cell: current status and future outlook," *Mater Today Chem*, vol. 22, p. 100595, Dec. 2021, doi: 10.1016/J.MTCHEM.2021.100595.

[26]   J. Liu *et al.*, "Low-temperature, solution processed metal sulfide as an electron transport layer for efficient planar perovskite solar cells," *J Mater Chem A Mater*, vol. 3, no. 22, pp. 11750–11755, May 2015, doi: 10.1039/C5TA01200G.

[27]   W. Ke *et al.*, "Effects of annealing temperature of tin oxide electron selective layers on the performance of perovskite solar cells," *J Mater Chem A Mater*, vol. 3, no. 47, pp. 24163–24168, Nov. 2015, doi: 10.1039/C5TA06574G.

[28]   Q. Dong *et al.*, "Insight into perovskite solar cells based on SnO2 compact electron-selective layer," *Journal of Physical Chemistry C*, vol. 119, no. 19, pp. 10212–10217,   May   2015,   doi: 10.1021/ACS.JPCC.5B00541/ASSET/IMAGES/LARGE/JP-2015-005419_0010.JPEG.

[29]   W. Ke *et al.*, "Lowerature solution-processed tin oxide as an alternative electron transporting layer for efficient perovskite solar cells," *J Am Chem Soc*, vol. 137,   no.   21,   pp.   6730–6733,   Jun.   2015,   doi: 10.1021/JACS.5B01994/SUPPL_FILE/JA5B01994_SI_001.PDF.

[30]   J. Li *et al.*, "Enhanced Crystallinity of Low-Temperature Solution-Processed SnO2 for Highly Reproducible Planar Perovskite Solar Cells," *ChemSusChem*, vol. 11, no. 17, pp. 2898–2903, Sep. 2018, doi: 10.1002/CSSC.201801433.

[31]   Z. Zhu *et al.*, "Enhanced Efficiency and Stability of Inverted Perovskite Solar Cells Using Highly Crystalline SnO2 Nanocrystals as the Robust Electron-Transporting Layer," *Advanced Materials*, vol. 28, no. 30, pp. 6478–6484, Aug. 2016, doi: 10.1002/ADMA.201600619.

[32]   Y. Wang *et al.*, "Performance Enhancement of Inverted Perovskite Solar Cells Based on Smooth and Compact PC61BM:SnO2 Electron Transport Layers," *ACS Appl Mater Interfaces*, vol. 10, no. 23, pp. 20128–20135, Jun. 2018, doi: 10.1021/ACSAMI.8B03444/ASSET/IMAGES/LARGE/AM-2018-03444S_0004.JPEG.

[33]   Q. Dong, Y. Shi, C. Zhang, Y. Wu, and L. Wang, "Energetically favored formation of SnO2 nanocrystals as electron transfer layer in perovskite solar cells with high efficiency exceeding 19%," *Nano Energy*, vol. 40, pp. 336–344, Oct. 2017, doi: 10.1016/J.NANOEN.2017.08.041.

[34]   Z. Liu, K. Deng, J. Hu, and L. Li, "Coagulated SnO2 Colloids for High-Performance Planar Perovskite Solar Cells with Negligible Hysteresis and Improved Stability," *Angewandte Chemie International Edition*, vol. 58, no. 33, pp. 11497–11504, Aug. 2019, doi: 10.1002/ANIE.201904945.

[35]   G. Yang *et al.*, "Effective Carrier-Concentration Tuning of SnO2 Quantum Dot Electron-Selective Layers for High-Performance Planar Perovskite Solar Cells," *Advanced Materials*, vol. 30, no. 14, p. 1706023, Apr. 2018, doi: 10.1002/ADMA.201706023.

[36]   Q. Jiang *et al.*, "Planar-Structure Perovskite Solar Cells with Efficiency beyond 21%," *Advanced Materials*, vol. 29, no. 46, p. 1703852, Dec. 2017, doi: 10.1002/ADMA.201703852.

[37]   Q. Jiang *et al.*, "Surface passivation of perovskite film for efficient solar cells," *Nature Photonics 2019 13:7*, vol. 13, no. 7, pp. 460–466, Apr. 2019, doi: 10.1038/s41566-019-0398-2.

[38]   Y. Wang *et al.*, "Interface Engineering of High-Performance Perovskite Photodetectors Based on PVP/SnO2 Electron Transport Layer," *ACS Appl Mater Interfaces*, vol. 10, no. 7, pp. 6505–6512, Feb. 2018, doi: 10.1021/ACSAMI.7B18511/ASSET/IMAGES/AM-2017-18511K_M003.GIF.

[39]   D. Yang *et al.*, "High efficiency planar-type perovskite solar cells with negligible hysteresis using EDTA-complexed SnO2," *Nature Communications 2018 9:1*, vol. 9, no. 1, pp. 1–11, Aug. 2018, doi: 10.1038/s41467-018-05760-x.

[40]   P. Zhu *et al.*, "Simultaneous Contact and Grain-Boundary Passivation in Planar Perovskite Solar Cells Using SnO2-KCl Composite Electron Transport Layer," *Adv Energy Mater*, vol. 10, no. 3, p. 1903083, Jan. 2020, doi: 10.1002/AENM.201903083.

[41]   M. Park, J. Y. Kim, H. J. Son, C. H. Lee, S. S. Jang, and M. J. Ko, "Low-temperature solution-processed Li-doped SnO2 as an effective electron transporting layer for high-performance flexible and wearable perovskite solar cells," *Nano Energy*, 2016, doi: 10.1016/j.nanoen.2016.04.060.

[42]   J. Song, X. Xu, J. Wu, and Z. Lan, "Low-temperature solution-processing high quality Nb-doped SnO2 nanocrystals-based electron transport layers for efficient planar perovskite solar cells," *Functional Materials Letters*, 2019, doi: 10.1142/S1793604718500911.

[43]   Z. Ma *et al.*, "Negligible hysteresis planar perovskite solar cells using Ga-doped SnO2 nanocrystal as electron transport layers," *Org Electron*, 2019, doi: 10.1016/j.orgel.2019.05.011.

[44]   Z. Xu *et al.*, "La-doped SnO2 as ETL for efficient planar-structure hybrid perovskite solar cells," *Org Electron*, vol. 73, no. March, pp. 62–68, 2019, doi: 10.1016/j.orgel.2019.03.053.

[45]   J. Tian, J. Zhang, X. Li, B. Cheng, J. Yu, and W. Ho, "Low-Temperature-Processed Zr/F Co-Doped SnO2 Electron Transport Layer for High-Efficiency Planar Perovskite Solar Cells," *Solar RRL*, vol. 4, no. 6, p. 2000090, Jun. 2020, doi: 10.1002/SOLR.202000090.

[46]   X. Huang *et al.*, "Polyelectrolyte-Doped SnO2 as a Tunable Electron Transport Layer for High-Efficiency and Stable Perovskite Solar Cells," *Solar RRL*, vol. 4, no. 1, pp. 1–8, 2020, doi: 10.1002/solr.201900336.

[47]   L. Dong *et al.*, "NaCl-passivated and Na+-doped tin oxide electron transport layers enable highly efficient planar perovskite solar cells," *Journal of Physics and Chemistry of Solids*, vol. 158, p. 110250, Nov. 2021, doi: 10.1016/J.JPCS.2021.110250.

[48]   J. Chen *et al.*, "Graphitic carbon nitride doped SnO2 enabling efficient perovskite solar cells with PCEs exceeding 22%," *J Mater Chem A Mater*, vol. 8, no. 5, pp. 2644–2653, Feb. 2020, doi: 10.1039/C9TA11344D.

[49]   Y. W. Noh, J. H. Lee, I. S. Jin, S. H. Park, and J. W. Jung, "Tailored electronic properties of Zr-doped SnO2 nanoparticles for efficient planar perovskite solar cells with marginal hysteresis," *Nano Energy*, vol. 65, p. 104014, Nov. 2019, doi: 10.1016/J.NANOEN.2019.104014.

[50]   J. Song, W. Zhang, D. Wang, K. Deng, J. Wu, and Z. Lan, "Colloidal synthesis of Y-doped SnO2 nanocrystals for efficient and slight hysteresis planar perovskite solar cells," *Solar Energy*, vol. 185, no. April, pp. 508–515, 2019, doi: 10.1016/j.solener.2019.04.084.

[51]   S. Chapagain *et al.*, "High Performing Inverted Flexible Perovskite Solar Cells via Solution Phase Deposition of Yttrium-Doped SnO2 Directly on Perovskite," *ACS Appl Energy Mater*, vol. 6, no. 9, pp. 4496–4502, May 2023, doi: 10.1021/ACSAEM.2C03720/ASSET/IMAGES/LARGE/AE2C03720_0005.JPEG.

[52]   X. Huang *et al.*, " Polyelectrolyte-Doped SnO 2 as a Tunable Electron Transport Layer for High-Efficiency and Stable Perovskite Solar Cells ," *Solar RRL*, 2020, doi: 10.1002/solr.201900336.

[53]   X. Zhou *et al.*, "Solution-processed Cu-doped SnO2 as an effective electron transporting layer for High-Performance planar perovskite solar cells," *Appl Surf Sci*, vol. 584, p. 152651, May 2022, doi: 10.1016/J.APSUSC.2022.152651.

[54]   R. Wang *et al.*, "Gadolinium-doped SnO2 electron transfer layer for highly efficient planar perovskite solar cells," *J Power Sources*, vol. 544, p. 231870, Oct. 2022, doi: 10.1016/J.JPOWSOUR.2022.231870.

[55]   H. Gu *et al.*, "CuCl2-modified SnO2 electron transport layer for high efficiency perovskite solar cells," *Nanotechnology*, vol. 34, no. 30, p. 305401, May 2023, doi: 10.1088/1361-6528/ACCFA3.

[56]   X. Liu *et al.*, "Stacking n-type layers: Effective route towards stable, efficient and hysteresis-free planar perovskite solar cells," *Nano Energy*, vol. 44, pp. 34–42, Feb. 2018, doi: 10.1016/J.NANOEN.2017.11.069.

[57]   M. Hu *et al.*, "Electron Transporting Bilayer of SnO2 and TiO2 Nanocolloid Enables Highly Efficient Planar Perovskite Solar Cells," *Solar RRL*, vol. 4, no. 1, p. 1900331, Jan. 2020, doi: 10.1002/SOLR.201900331.

[58]   Y. W. Noh, J. H. Lee, I. S. Jin, S. H. Park, and J. W. Jung, "Tailored electronic properties of Zr-doped SnO2 nanoparticles for efficient planar perovskite solar cells with marginal hysteresis," *Nano Energy*, vol. 65, p. 104014, Nov. 2019, doi: 10.1016/J.NANOEN.2019.104014.

[59]   D. Wang *et al.*, "ZnO/SnO2 Double Electron Transport Layer Guides Improved Open Circuit Voltage for Highly Efficient CH3NH3PbI3-Based Planar Perovskite Solar Cells," *ACS Appl Energy Mater*, vol. 1, no. 5, pp. 2215–2221, May 2018, doi: 10.1021/ACSAEM.8B00293/ASSET/IMAGES/LARGE/AE-2018-00293F_0006.JPEG.

[60]   L. Lin *et al.*, "ZnO-Modified Anode for High-Performance SnO2-Based Planar Perovskite Solar Cells," *ACS Appl Energy Mater*, vol. 2, no. 10, pp. 7062–7069, Oct. 2019, doi: 10.1021/ACSAEM.9B00845/ASSET/IMAGES/LARGE/AE9B00845_0006.JPEG.

[61]   D. Wang *et al.*, "To Greatly Reduce Defects via Photoannealing for High-Quality Perovskite Films," *ACS Appl Mater Interfaces*, vol. 11, no. 23, pp. 20943–20948, Jun. 2019, doi: 10.1021/ACSAMI.9B06873/ASSET/IMAGES/MEDIUM/AM-2019-06873D_M004.GIF.

[62]   J. Dagar, S. Castro-Hermosa, G. Lucarelli, F. Cacialli, and T. M. Brown, "Highly efficient perovskite solar cells for light harvesting under indoor illumination via solution processed SnO2/MgO composite electron transport layers," *Nano Energy*, vol. 49, pp. 290–299, Jul. 2018, doi: 10.1016/J.NANOEN.2018.04.027.

[63]   J. Song, E. Zheng, X. F. Wang, W. Tian, and T. Miyasaka, "Low-temperature-processed ZnO–SnO2 nanocomposite for efficient planar perovskite solar cells," *Solar Energy Materials and Solar Cells*, vol. 144, pp. 623–630, Jan. 2016, doi: 10.1016/J.SOLMAT.2015.09.054.

[64]   Y. Hou *et al.*, "A Band-Edge Potential Gradient Heterostructure to Enhance Electron Extraction Efficiency of the Electron Transport Layer in High-Performance Perovskite Solar Cells," *Adv Funct Mater*, vol. 27, no. 27, p. 1700878, Jul. 2017, doi: 10.1002/ADFM.201700878.

[65]   M. Kohan, T. Mahmoudi, Y. Wang, Y. H. Im, and Y. B. Hahn, "SnO2/BaSnO3 electron transport materials for stable and efficient perovskite solar cells," *Appl Surf Sci*, vol. 613, p. 156068, Mar. 2023, doi: 10.1016/J.APSUSC.2022.156068.

[66]   Z. Xu, X. Zhou, X. Li, and P. Zhang, "Polymer-Regulated SnO2 Composites Electron Transport Layer for High-Efficiency n–i–p Perovskite Solar Cells," *Solar RRL*, vol. 6, no. 8, p. 2200092, Aug. 2022, doi: 10.1002/SOLR.202200092.

[67]   L. Zhang *et al.*, "Amorphous F-doped TiOx Caulked SnO2 Electron Transport Layer for Flexible Perovskite Solar Cells with Efficiency Exceeding 22.5%," *Adv Funct Mater*, vol. 33, no. 11, p. 2213961, Mar. 2023, doi: 10.1002/ADFM.202213961.

[68]   K. Zhang *et al.*, "Modifying the photoelectric performance of SnO2 via D-arginine monohydrochloride for high-performance perovskite solar cells," *J Alloys Compd*, vol. 946, p. 169361, Jun. 2023, doi: 10.1016/J.JALLCOM.2023.169361.

[69]   Z. Li *et al.*, "In-situ peptization of WO3 in alkaline SnO2 colloid for stable perovskite solar cells with record fill-factor approaching the shockley–queisser limit," *Nano Energy*, vol. 100, p. 107468, Sep. 2022, doi: 10.1016/J.NANOEN.2022.107468.

[70]   K. Parvez, *Two-dimensional nanomaterials: Crystal structure and synthesis*. Elsevier Inc., 2019. doi: 10.1016/B978-0-12-815889-0.00001-5.

[71]   K. Mahmood, A. Khalid, S. W. Ahmad, H. G. Qutab, M. Hameed, and R. Sharif, "Electrospray deposited MoS2 nanosheets as an electron transporting material for high efficiency and stable perovskite solar cells," *Solar Energy*, vol. 203, pp. 32–36, Jun. 2020, doi: 10.1016/J.SOLENER.2020.04.021.

[72]   S. Asaithambi *et al.*, "Synthesis and characterization of various transition metals doped SnO2@MoS2 composites for supercapacitor and photocatalytic applications," *J Alloys Compd*, vol. 853, p. 157060, Feb. 2021, doi: 10.1016/J.JALLCOM.2020.157060.

[73]   S. Singh, R. M. Sattigeri, S. Kumar, P. K. Jha, and S. Sharma, "Superior Room-Temperature Ammonia Sensing Using a Hydrothermally Synthesized MoS2/SnO2Composite," *ACS Omega*, vol. 6, no. 17, pp. 11602–11613, May 2021, doi:
10.1021/ACSOMEGA.1C00805/ASSET/IMAGES/LARGE/AO1C00805_0009.JP EG.

[74]   G. Muthulakshmi, M. Mohamed Ismail, R. Ramya, M. Arivanandhan, S. Arjunan, and A. Bhaskaran, "Facile preparation of SnO2/MoS2 nanocomposites with high electrochemical performance for energy storage applications," *Inorg Chem Commun*, vol. 143, p. 109802, Sep. 2022, doi: 10.1016/J.INOCHE.2022.109802.

[75]   X. Ni, C. Chen, Q. Wang, and Z. Li, "One-step hydrothermal synthesis of SnO2-MoS2 composite heterostructure for improved visible light photocatalytic performance," *Chem Phys*, vol. 525, p. 110398, Sep. 2019, doi: 10.1016/J.CHEMPHYS.2019.110398.

Chapter 3

Review of Experimentation Characterization & Testing Methods

The following chapter includes the outline of all the experimentation, characterization and testing techniques used in this research work.

3.1 Synthesis Method of Nanoparticle

To synthesize the nanoparticles of the two methods were used. The first is the solution processing technique and the second is the refluxing method.

3.1.1 Refluxing

The process of Refluxing involves the formation of the vapors, condensation of vapors followed by the return of the condensed vapors back into the system from where they were originated. For this purpose, the temperature of the system where the solution is being heated is kept high above its boiling point. This allows the formation of vapors followed. To condense the vapors, the cooling system is attached within the system. As the vapors are produced, they rose above where a water-cooling system reduced their temperature resulting in the returning of the vapors back into the system. As a result of refluxing, the formation of reactant into the products is assured by speeding up the kinetics of the system while cooling system makes sure that the temperature of the solvent does not rises beyond the limit where it becomes hazardous enough to catch fire [1].
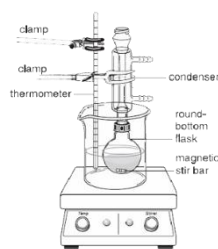
Figure 3.1: Refluxing Apperatus [1]

3.1.2 Solution Processing

It is one of the most widely used methods because of the facile processing of the Tin Oxide. The method includes the mixing the of the salt and the solvent and the desired product is achieved by controlling various other factor such as stirring time, temperature, pH, molarity aging of the solution. Sometimes, the solution can be mixed with the other solution to adjust their pH. After the initial stage of the stirring is complete, it could be followed by the aging of the solution of the solution for the desired period.

3.1.3 Spin Coating

It is one of the convenient method for deposition of thin films. In this method, the solution is dropped on the substrate which is then rotated at desired speed and acceleration for specific period. All these parameters define the thickness of the film. By adjusting these parameters, the desired thickness for the film can be achieved which can range few micrometers to several nanometers. In order to deposit the film, the substrate upon which the film is to be deposited, is placed inside the spin coater and is held by vacuum being generated by the pump. The time and the speed can be controlled by the built-in time and speed function. The thickness of the film has an inverse dependance on the spin speed along with some other variables such as evaporation rate of the solvent, its viscosity, concentration, and temperature of the substrate [2].
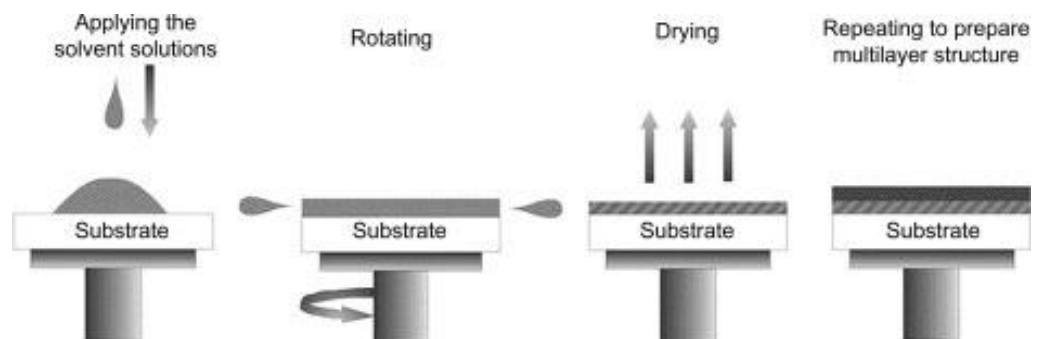
Figure 3.2: Steps of Spin Coating [3]

3.1.4   Spin Methods

The spin methods can be divided into two methods. The first is the Static Spin Coating and the second is the Dynamic Spin Coating.

3.1.1.1   Dynamic Spin Coating

In dynamic spin coating, the solution is dropped on the substrate after it reaches the desired spin speed. The solution should be dropped in a quick and uniform manner while the centripetal force and the spin speed ensures the smooth and uniform coating on the substrate [4].

3.1.1.2   Static Spin Coating

This method is generally preferrable when the spin speed is 1000 or below 1000 RPM. In this method, the solvent is first dropped on to the substrate after it is being placed inside the spin coater and this step is followed by applying spinning the substrate to achieve the desired coating [4].

Figure 3.3: Process of Static & Dynamic Spin Coating [5]

3.1.5   Advantages

  i. The technique is simple and facile.
 ii. As a result of high speed, the film dries rapidly.
iii. Thin films can be deposited on a wide variety of range of thickness.

3.1.6 Disadvantages

i. The technique is not suitable for mass fabrication as it involves the use of single substrate at a time.

ii. Most of the solution is wasted as a result of being thrown away at high speed and the actual amount of solution that is being utilized is only 10%.

iii. The quick drying process of spin coating can lead to lower performance in some nano technologies.

3.2 Characterization and Testing Techniques

3.2.1 XRD

It is a non-destructive technique that is used for the identification of phases of crystalline material along with providing information about the unit cell dimension. In addition to this it also provides information about the type of lattice mismatch information between substrate and film, crystal structure, their orientation, defects in the crystal structure along with the measurement of stress and strain in the crystal [6].

The principle on which XRD works is Bragg's Law. It uses monochromatic wavelength of X-rays which are directed towards the sample. Upon the interaction of the X-rays and the sample interference is produced. If the material is crystalline then it results in the constructive interference thus satisfying the Bragg's Law which is stated below

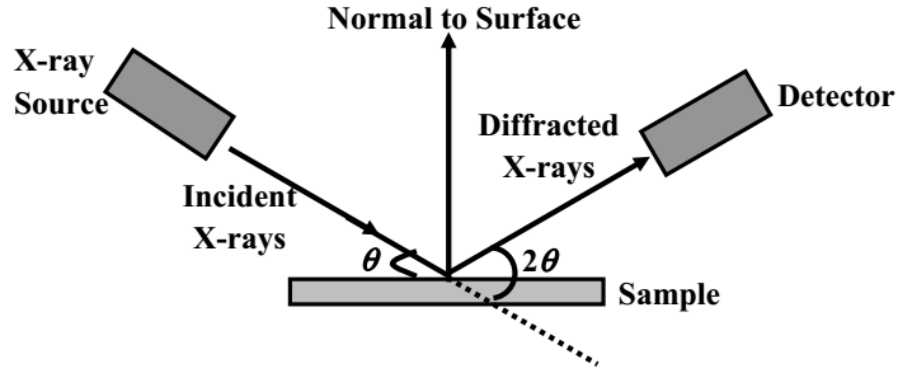$$n\lambda = 2d \sin \theta \qquad (3.1)$$

Figure 3.4:XRD schematic diagram [7]

where 'n' is the number of integers, 'd' is the spacing between crystal planes, 'λ' is the wavelength of the X-rays and 'θ' is the angle between the reflected and incident beam. When constructive interference occurs, the diffraction is observed, detected, and counted after being processed. After the diffraction is converted into d-spacing, the mineral is identified which is achieved after the pattern obtained is compared with the reference pattern. Beside this to find the crystallite size of the crystals the following equation can be used [6]

$$D = 0.9\lambda / \beta cos\theta \qquad (3.2)$$

where 'D' is the crystallite size, 'λ' is the wavelength in nm, 'θ'' is the diffraction pattern, and 'β' is the full width half maximum (FWHM).

3.2.2   Scanning Electron microscopy (SEM): -

SEM uses an electron beam instead of light. This high energy electron beam is focused on the sample. Since instead of photons of light the electrons are used therefore this allows to bring in the fine details and an electron can pass through places where photons of light cannot pass because of their bigger size [8].

The electrons are generated with the help of the electron guns which consist of anode and cathode. After the electrons are generated, they are controlled with the help of set of condenser lens while they are travelling down the column while they focus the beam on to the spot on the sample. After the condenser lens, the beam of electron is further controlled with the help of the deflection coil, which deflects the electron

beam properly on to the sample. The signals generated can be viewed on the detector [8].
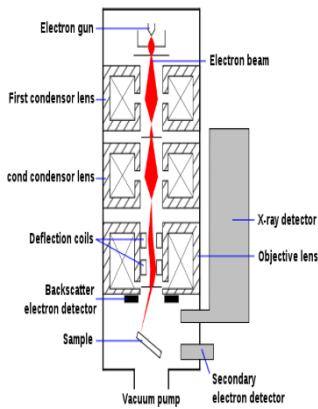
Figure 3.5: Schematic of an SEM [9]

After they strike the sample different type of signals are generated which carry information regarding morphology of the film, its chemical composition. Different types of signals that are generated are shown below in Figure 3.6. All these signals are detected by using different type of detectors to extract different type of information that they are carrying. The secondary electrons provide information about the morphology of the film while the backscattered electrons are used to determine the elemental composition of the material [10].
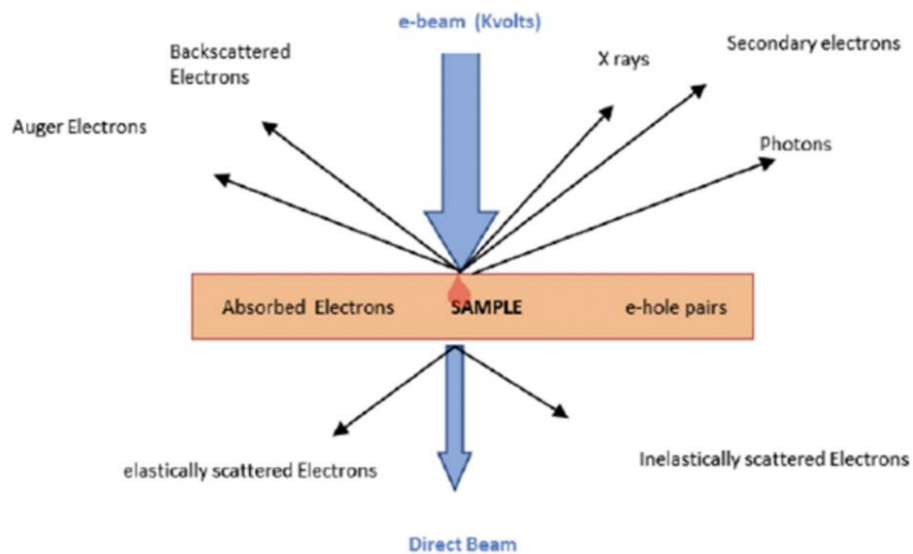
Figure 3.6: Signals generated during a SEM analysis [11]

3.2.3 Energy Dispersive Spectroscopy (EDS/EDX)

It is an analytical and quantitative technique which provides information about the chemical composition of the material along with its chemical characterization. It is generally used in addition with the SEM and uses X-rays which are generated as a result of the interaction between the electron beam and sample under consideration [12].

When the sample is bombarded with the electron beam, then due to its high energy some of the electrons are knocked out of the surface of the material while some of the samples are excited are at the same time along with the creation of the vacancies. When these electrons jump back into the lower energy shells, they emit signals in the form of the X-rays. These signals are unique for each element and are detected by the detector thus providing useful information about the elemental composition of the material [13].

3.2.4 Hall Effect Measurement

Based on the Hall effect discovered by Edwin Hall in 1879, the hall effect measurements are used to calculate carrier type, mobility, density, sheet resistivity and charge carrier concentration of a semi-conductor material. Hall effects are observed whenever the conductor is placed perpendicular to a magnetic field. This result in the generation of voltage which is transverse to the electric current in the conductor [14].

Figure 3.7: Flow of Charges via Hall Effect [15]

The right-hand rule can be used to find the direction of the magnetic field applied. So, whenever the magnetic field is applied, the charge experience both electrical and ma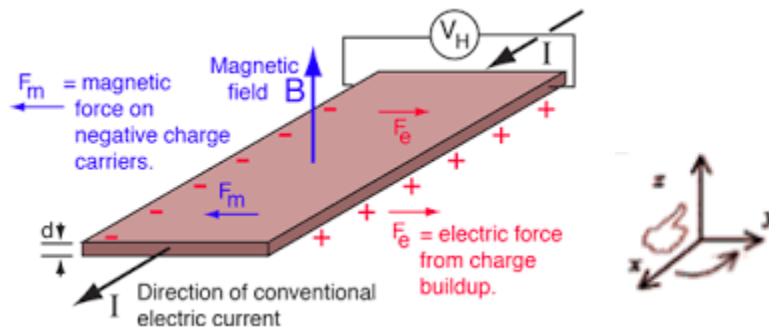gnetic forces resulting in the production of Hall voltage. The force experienced by the charges is known as Lorentz force and is given as [16]

$$F = q(E + v \, x \, B) \tag{3.3}$$

Where E is the Electrical Field, B is the magnetic field and q is the charge. With the help of Hall voltage, the charge density can be calculated as

$$ns = IB/qlVHl \tag{3.4}$$

The Hall coefficient is negative for n-type charges and positive for p-type charges. There two different methods that are used for the hall effect calculation. The first one is the Van der Pauw while the second one is the Hall Bar method. Originally Hall Bar method was used and consist of six point contact, however in comparison to this Van der Pauw method much more facile and easy method and use four points instead of six points. In case of Van der Pauw, the sheet resistance can be calculated by using the following equation [17,18]

$$exp(-\pi RA/RS) + exp(-\pi RB/RS) = 1 \tag{3.5}$$

While mobility can be calculated as

$$\eta = 1/(qnsRs) \tag{3.6}$$

In addition to the above-mentioned parameters, the Hall effect ca also be used to calculate the IR or IV curve. To obtain better results while using Van der Pauw method the sample must have followed properties:

- The coating on the sample should be uniform.
- The ohmic contacts on the sample should be properly formed.
- The thickness of the sample should also be known.

3.2.5   Ultraviolet Visible Spectroscopy (UV-Vis)

The UV-Vis is a quantitative method that measures the amount of light that is absorbed by the material. Information about three different parameters is provided by UV-Vis which includes its Transmittance, Absorption and Reflection. The

spectrum range that is used by the UV-Vis lies in the range of 190 nm- 4000/185-3300 nm thus covering range from UV to Far Infrared, however the most observed spectrum is the visible spectrum the covers the range in between 400 nm-700 nm [19].

With the help of parameters above that are provided by the UV-Vis, information of various nature can be calculated and observed. In a quantitative manner the information provided by the absorption spectra can be used to identify the functional group or a certain chemical by matching its absorption spectra with the reference spectra. Also, with the help of absorption spectra the band gap of a semiconductor can also be calculated. Beside this by repeating the UV-Vis analysis over time the kinetics of a rection can also be identified [19].
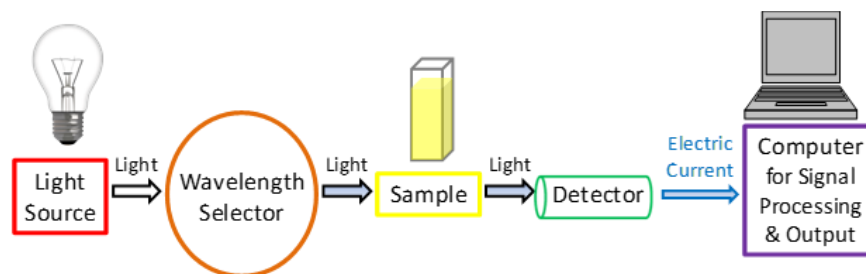
Figure 3.8: A simplified schematic of UV-Vis [20]

3.2.6   IV-Curve Measurement

Generally, an IV curve is a test in which is subjected to electrical devices. In this test, a range of voltages is applied to the device and the current flown against each voltage is measured and plotted with voltage on the x-axis and current on the y-axis. Each type of electrical load such as resistor, diode etc., have their characteristics IV character [21].

In case of solar cell, IV-curve measurement are used to find out the efficiency of solar cell or how well the fabricated solar cell is working which depends on different parameters such as its active area, exciton dissociation, charge separation and charge injection. Under dark conditions, the behavior of the solar cell is similar to that of a diode. However, when illuminated with a light source, then IV curve provides

information about the how effectively the cell is working and this is determined with the help of the parameters that are provided by the IV-curve which includes Isc, Voc, Imp, Vmp and Fill Factor [22].
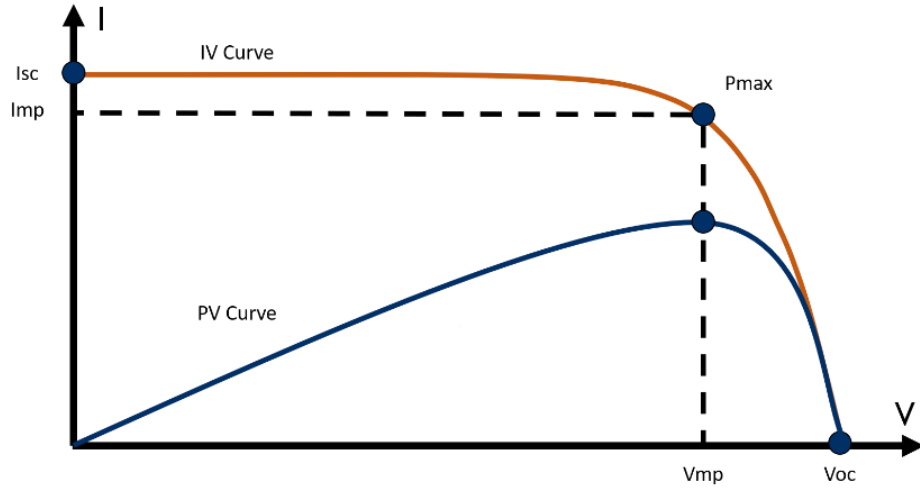
Figure 3.9: An IV-curve of a solar cell [23]

Summary

The chapter highlights the methods that have been used for synthesis of SnO_2 along with the techniques that have been used for its deposition and characterization. The characterization techniques that are used include OM, SEM, XRD, Hall Effect, EDX, UV-Vis and IV-curve. OM provides information about morphology at different resolution depending upon its lenses while SEM provides information at higher resolution which includes topography, morphology, and surface defects at nano structural level. EDS provides information about elemental composition present in the sample under consideration while XRD provides information about the crystallinity of the structure along with its various phases. While UV-Vis is used to measure transmittance and absorbance, the Hall Effect is used to measure the conductivity, charge carrier concentration and charge carrier mobility of the charges. Finally, IV-curve tracer is used to measure the performance of the solar cell fabricated by using illumination under one sun.

References

[3]   A. Mishra, N. Bhatt, and A. K. Bajpai, "Nanostructured superhydrophobic coatings for solar panel applications," *Nanomaterials-Based Coatings: Fundamentals and Applications*, pp. 397–424, Jan. 2019, doi: 10.1016/B978-0-12-815884-5.00012-0.

[2]   Ossila, "Spin Coating: Complete Guide to Theory and Techniques | Ossila." https://www.ossila.com/pages/spin-coating (accessed Jan. 25, 2022).

[1]   UTSC, "What is Refluxing?" https://www.utsc.utoronto.ca/webapps/chemistryonline/production/reflux.php (accessed Jan. 19, 2022).

[4]   CSI, "Spin Coating - Techniques & Uses | Coating Systems." https://coatingsystems.com/apply-spin-coating/ (accessed Jan. 25, 2022).

[5]   Y. Ma *et al.*, "Controlled Growth of CH3NH3PbI3 Using a Dynamically Dispensed Spin-Coating Method: Improving Efficiency with a Reproducible PbI2 Blocking Layer," *ChemSusChem*, vol. 10, no. 12, pp. 2677–2684, Jun. 2017, doi: 10.1002/CSSC.201700449.

[6]   Carleton, "X-ray Powder Diffraction (XRD)." https://serc.carleton.edu/research_education/geochemsheets/techniques/XRD.html (accessed Jan. 25, 2022).

[7]   W. W. Andualem, "GREEN SYNTHESIS OF CUO NANOPARTICLES FOR THE APPLICATION OF DYE SENSITIZED SOLAR CELL," *Certified Journal │ 29 Andualem. World Journal of Pharmaceutical Research www.wjpr.net │*, vol. 9, p. 30, 2020, doi: 10.20959/wjpr202013-18436.

[8]   C. Woodford, "How do electron microscopes work? - Explain that Stuff." https://www.explainthatstuff.com/electronmicroscopes.html (accessed Jan. 25, 2022).

[9]   "Scanning   Electron   Microscopy   -   Nanoscience   Instruments."
https://www.nanoscience.com/techniques/scanning-electron-microscopy/
(accessed Jul. 17, 2023).

[10]   A. Nanakoudis, "Scanning Electron Microscopy - SEM - Accelerating
Microscopy."   https://www.thermofisher.com/blog/microscopy/what-is-sem-
scanning-electron-microscopy-explained/ (accessed Jan. 25, 2022).

[11]   "What   is   an   Electron   Microscope?   -   HORIBA."
https://www.horiba.com/fra/cathodoluminescence-spectroscopy-electron-
microscope/ (accessed Jul. 17, 2023).

[12]   A. Nanakoudis, "EDX Analysis - SEM - EDS Analysis - Accelerating
Microscopy." https://www.thermofisher.com/blog/microscopy/edx-analysis-with-
sem-how-does-it-work/ (accessed Jan. 25, 2022).

[13]   J.   Goodge,   "Energy-dispersive   detector   (EDS)."
https://serc.carleton.edu/research_education/geochemsheets/eds.html   (accessed
Jan. 25, 2022).

[14]   L.   Learning,   "The   Hall   Effect | Physics."
https://courses.lumenlearning.com/physics/chapter/22-6-the-hall-effect/ (accessed
Jan. 25, 2022).

[15]   "Hall   Effect."   http://hyperphysics.phy-astr.gsu.edu/hbase/magnetic/Hall.html
(accessed Jul. 17, 2023).

[16]   Britannica, "Lorentz force | Equation, Properties, & Direction | Britannica."
https://www.britannica.com/science/Lorentz-force (accessed Jan. 25, 2022).

[17]   F. S. Oliveira, R. B. Cipriano, F. T. da Silva, E. C. Romão, and C. A. M. dos Santos,
"Simple analytical method for determining electrical resistivity and sheet resistance
using the van der Pauw procedure," *Scientific Reports 2020 10:1*, vol. 10, no. 1, pp.
1–8, Oct. 2020, doi: 10.1038/s41598-020-72097-1.

[18] "▷ What is the Van-der-Pauw measurement method?" https://www.linseis.com/en/methods/van-der-pauw-measurement/ (accessed Jan. 25, 2022).

[19] Justin Tom, "UV-Vis Spectroscopy: Principle, Strengths and Limitations and Applications | Technology Networks." https://www.technologynetworks.com/analysis/articles/uv-vis-spectroscopy-principle-strengths-and-limitations-and-applications-349865 (accessed Jan. 25, 2022).

[20] "UV-Vis Spectroscopy: Principle, Strengths and Limitations and Applications | Technology Networks." https://www.technologynetworks.com/analysis/articles/uv-vis-spectroscopy-principle-strengths-and-limitations-and-applications-349865 (accessed Jul. 17, 2023).

[21] Ossila, "I-V Curve Measurement | How to Measure Solar Cell I-V Curve | Ossila." https://www.ossila.com/pages/iv-curves-measurement (accessed Jan. 25, 2022).

[22] P. Education, "IV Curve | PVEducation." https://www.pveducation.org/pvcdrom/solar-cell-operation/iv-curve (accessed Jan. 25, 2022).

[23] "What is a PV Module IV Curve? - Atonometrics." https://www.atonometrics.com/applications/what-is-a-pv-module-iv-curve/ (accessed Jul. 17, 2023).

Chapter 4
Materials and Methodology

A series of experiments were conducted for the research work. To meet the research goals, the experiments sequence is defined in the following order:

i.   Synthesis of Tin oxide

ii.   Synthesis of Tin oxide and MoS_2 Composite

iii.   Synthesis of Perovskite Absorber Layer

iv.   Synthesis of Hole Transport Layer

v.   Fabrication of Perovskite Solar Cell

4.1   Materials

Tin Chloride Dihydrate ($SnCl_2.2H_2O$, 99.99%), Cesium Bromide (CsBr, 99.9%) and Lead iodide (PbI_2, 99.99%) were purchased from Sigma-Aldrich. All solvents including Absolute Ethanol, IPA, Acetone N-dimethylformamide (DMF, anhydrous 99.8%), Dimethyl Sulfoxide (DMSO, 99.8%), and chlorobenzene (CB, anhydrous 99.8%) and Chlorobenzene (C) were also purchased from Sigma Aldrich. The Pristine Nanoflakes of MoS_2 were purchased from Graphene Super Market (>99%). Methylammonium iodide (MAI) was bought from Solaronix. Super P. Carbon Black (CB) and Graphite was purchased from MTI Corporation. All the analytical grade materials were used without any further purification.

4.2   Fabrication of Electron Transport Layer

4.2.1   Synthesis of SnO_2

The SnO_2 solution was prepared by refluxing process following the method in [1]. Briefly $SnCl_2.2H_2O$ was dissolved in Absolute Ethanol to prepare 0.1M solution. For this purpose, 1.128g of $SnCl_2.2H_2O$ was dissolved in round bottom flask. The solution was refluxed for 3 hours at 80° C using oil bath heating. Then the solution was left to age for further 3 hours at 40° C to incorporate atmospheric oxygen into

solution to promote oxidation of Sn from Sn^{+2} to Sn^{+4}. After that the solution was left to stay in the dark to age for three days to promote nucleation.

4.2.2 Synthesis of SnO_2 and MoS_2 Composite

The Tin Oxide was prepared as mentioned in section 4.2.1. The MoS_2 flakes were sonicated for 1 hour before being used. The flakes were added in the SnO_2 solution in 10%, 20%, 30% and 40% (v/v %). After the addition the solution was stirred for 30 minutes at room temperature to form a homogenous mixture. After that the composition was deposited via spin coating using the parameters mentioned in Table 4.1.

Table 4.1: Deposition Parameters for Electron Transport Layer

Sr. No.	Sample Composition	rpm	Acceleration	Time (s)	Annealing Time (h)	Annealing Time (°C)
1	SnO_2	2000	2000	30	3	250
2	SnO_2 (90%)/MoS_2 (10%)	2000	2000	30	3	250
3	SnO_2 (80%)/MoS_2 (20%)	2000	2000	30	3	250
4	SnO_2 (70%)/MoS_2 (30%)	2000	2000	30	3	250

4.3 Synthesis of Perovskite Absorber Layer

For the deposition of perovskite with SnO_2-MoS_2 composite, CsBr doped absorber layer was prepared by mixing PbI_2 461.01 mg, MAI 143.01 mg and CsBr 21.282 mg was dissolved into the DMF: DMSO (4:1). The mixture was stirred overnight around 70° C. The precursor is prepared in the glove box at relative humidity of less

than 20%. After the stirring was completed, the solution was taken out for ambient deposition.

For the preparation of standard absorber layer for solar cell fabrication, PbI_2 461.01 mg and MAI 159 mg were mixed in 1:1 mixture was dissolved into the DMF: DMSO (4:1). To prepare the CsBr doped absorber layer PbI_2 461.01 mg, MAI 143.01 mg and CsBr 21.282 mg was dissolved into the DMF: DMSO (4:1). Both mixtures around were stirred at 70 ºC for 2 hours. The precursor is prepared in the glove box at relative humidity of less than 20%. After the stirring was completed, the solution was taken out for ambient deposition.

4.4　　Synthesis of Hole Transport Layer

4.4.1　Carbon-Graphite Paste

For the fabrication of half cells, the carbon paste was prepared in the following manner. The carbon-graphite paste (CGP) was used instead of traditional and expensive HTL materials. The synthesis of CGP is quite facile. To prepare the paste the Graphite and Carbon are mixed in 3:1 (wt %). Polyvinyl Acetate was also added into paste constituting 20% of paste by weight for preventing it from becoming brittle and being scratched off while being deposited on the cell. First polyvinyl acetate was dissolved in the chlorobenzene to achieve the desired viscosity. Then the mixture of CB and graphite was added into it and was ball milled using zirconia beads and vortex mixture for nearly five hours.

4.5　　Cell Fabrication

The FTO were etched by using Zinc powder and 1M HCl to remove the conductive coating. Then the FTO's were cleaned by sonicating them subsequently with Deionized Water, Isopropanol, Acetone and with Isopropanol again for 15 minutes each followed by drying them for 10 minutes at 100º C. This step was followed by plasma cleaning of substrate for 10 minutes by using Argon and oxygen plasma.

The solution of SnO_2 individually was first filtered using spin coated on to the FTO substrate at 2000 RPM for 30 seconds. After the deposition, the layer was annealed on hotplate at 250º C for 3 hours.

After the deposition of ETL, the slides were once again plasma cleaned for few minutes. Then the prepared precursor of the Perovskite Absorber Layer was deposited above ETL via spin coating in ambient environment at 4000 rpm for 30 seconds followed by annealing at 80º C for 40 minutes. Then the carbon mixture paste that was being prepared and deposited on Perovskite Absorber Layer via doctor blading. The layer was dried at 70º C for 40 minutes in the oven. After that, the performance of the cell was tested on the IV measurement setup equipped with solar simulator.

4.6   Characterization Techniques

The film's structural analysis involved the utilization of a Bruker D8 Advance X-ray Diffractometer with Cu Kα radiation (V = 40 kV, I = 30 mA, P = 1200 W, and λ = 1.548 Å) to assess its crystallinity. The film's surface morphology was examined through field electron scanning electron microscopy (SEM) employing a Zeiss 500VP with an acceleration voltage of 5 kV and field magnification ranging from 5 μm to 100 nm. To ascertain the material's bandgap and transmittance, a Shimadzu UV-3600i Plus spectrophotometer was employed. The steady-state photoluminescence (PL) analysis was conducted using an excitation wavelength of 450 nm on an iHR320 spectrophotometer provided by Horiba Scientific. The IV characteristics of the cells were evaluated using Newport Sol3A Class AAA Solar Simulators under 1 sun illumination. The measurement of the Hall Effect was carried out utilizing the ECOPIA HMS-3000 instrument. For the deposition of the films, the WS-650 MZ-23NPPB spin coater was used.

Summary

This chapter briefly summarizes the different materials that are being used for the synthesis of the different transport layers including ETL, Perovskite Absorber Layer and CGP. In addition to this, the methods for synthesis for each layer have also been discussed including all the parameters that are precisely required for the completion of reaction. After that, the complete procedure for the fabrication of cell long with all the parameters of the deposition is also discussed in the last section.

References

[1]   Q. Dong, Y. Shi, C. Zhang, Y. Wu, and L. Wang, "Energetically favored formation of SnO2 nanocrystals as electron transfer layer in perovskite solar cells with high efficiency exceeding 19%," *Nano Energy*, vol. 40, pp. 336–344, Oct. 2017, doi: 10.1016/J.NANOEN.2017.08.041.

Chapter 5

Results and Discussion

5.1.   SnO$_2$

The thin film of SnO$_2$ was deposited as mentioned in Chapter 4. The XRD analysis was performed and the XRD pattern is shown in Figure 5.1(c) which shows the formation of following phases (1 1 0), (1 0 1), (2 1 1), and (1 1 2) at 26.63º, 33.29 º and 51.62 º. These results are in good accordance with JCPDS file no. 77-0452. For a material serving its role as an ETL, it should exhibit high transmittance to allow maximum spectrum of light to pass through it. Since the maximum number of spectra that is reaching earth consist of visible spectrum, therefore ETL has to ensure that this spectrum should reach the perovskite absorber layer. SnO$_2$ is one of the widely used materials serving the role and being employed as ETL in perovskite solar cell. SnO$_2$ has a wide bandgap ranging from 3.6 eV – 4.1 eV[1]. Therefore, it exhibits good transparency in the visible spectrum.

The transmission spectra of SnO$_2$ is shown in Figure 5.1(a). Having a band gap of 3.993 eV as indicated by the Tauc plot in Figure 5.1(b), it has exhibited excellent average transparency of 90.1% in the visible spectrum ranging from 380 nm to 700 nm.
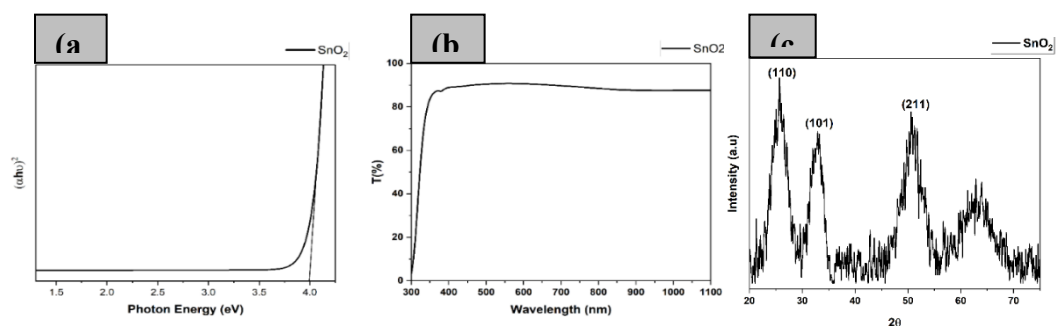

Figure 5.1: SnO$_2$ (a) Tauc Plot, (b) XRD & (c) Transmittance Spectra

5.2.   Molybdenum Disulfide (MoS$_2$)

MoS$_2$ is one of materials whose properties change along with its thickness. The single layer MoS$_2$ has shown different characteristics as compared to its bulk counterparts. In the current scenario, the pristine nano flakes of MoS$_2$ are being used as dopant. The solution of MoS$_2$ was being sonicated to obtain single layered pristine flakes. Various characterizations including UV-Vis, PL, Raman Spectroscopy are being used to verify these results in comparison to literature.
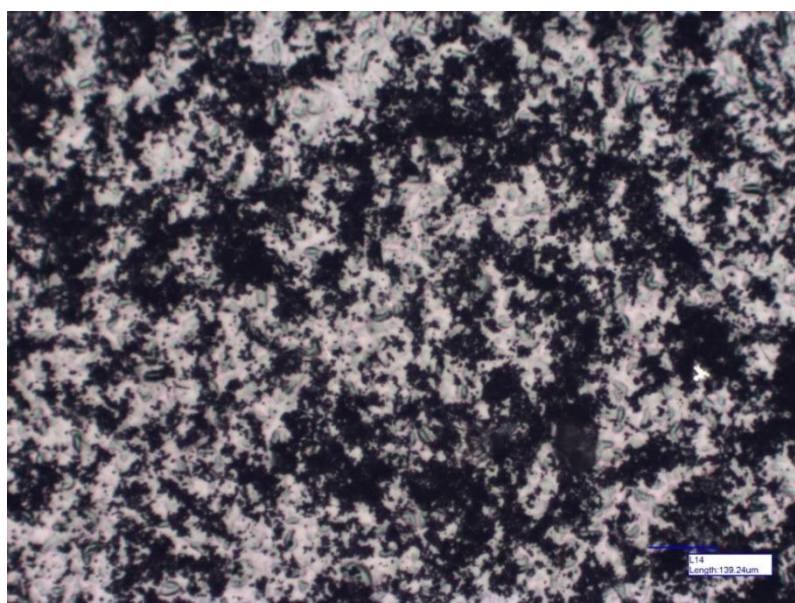

Figure 5.2: OM image of MoS$_2$ flakes deposited on FTO via drop casting and magnified at 20x

5.3.1.   UV-Vis of MoS$_2$

UV-Vis spectra of MoS$_2$ is shown Figure 5.3(a). The MoS$_2$ absorption spectra has shown its prominent peaks at 675 nm and 610 nm and represented by B and A respectively. This can be attributed to the direct exciton transition at Brillouin zone K point. Their energy difference is due to the spin-orbital splitting of the valence band, and the two resonances are known as A$_1$ and B$_1$ excitons respectively. The band gap edge is represented by the point C on Figure 5.3(a) and is calculated to be 2.42 eV via Tauc Plot as indicated in Figure 5.3(b).
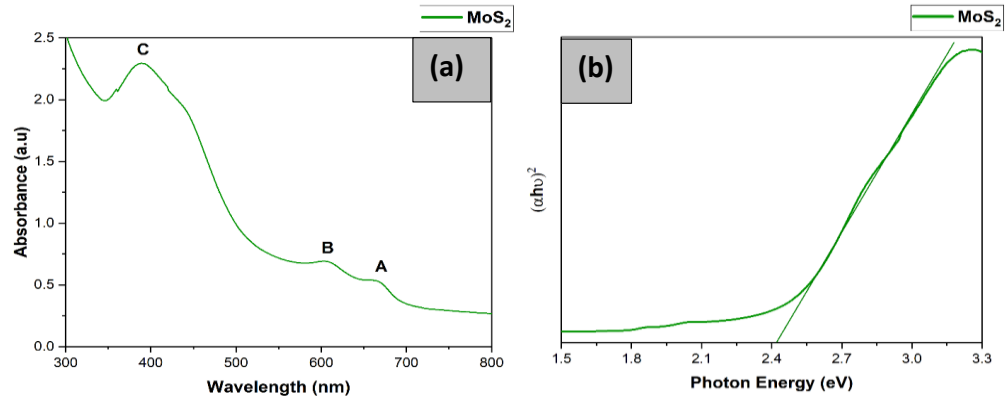
Figure 5.3: (a) MoS₂ flake giving of two intense peaks for its A and B exciton (b) Tauc Plot of MoS₂.

5.3.2. Photoluminescence of MoS₂

For thin layer MoS_2, there occurs a very little change in the absorption bands. However, the PL intensity of the MoS_2 also varies with its thickness and a significant effect can be observed. The single layer structure is known to give prominent PL emission peaks due to its direct band gap at the A and B exciton transitions. While with the increasing number of layers, the bandgap not only decreases but is also shifted from direct to indirect resulting in the lower or zero emission wavelength like in silicon [2].
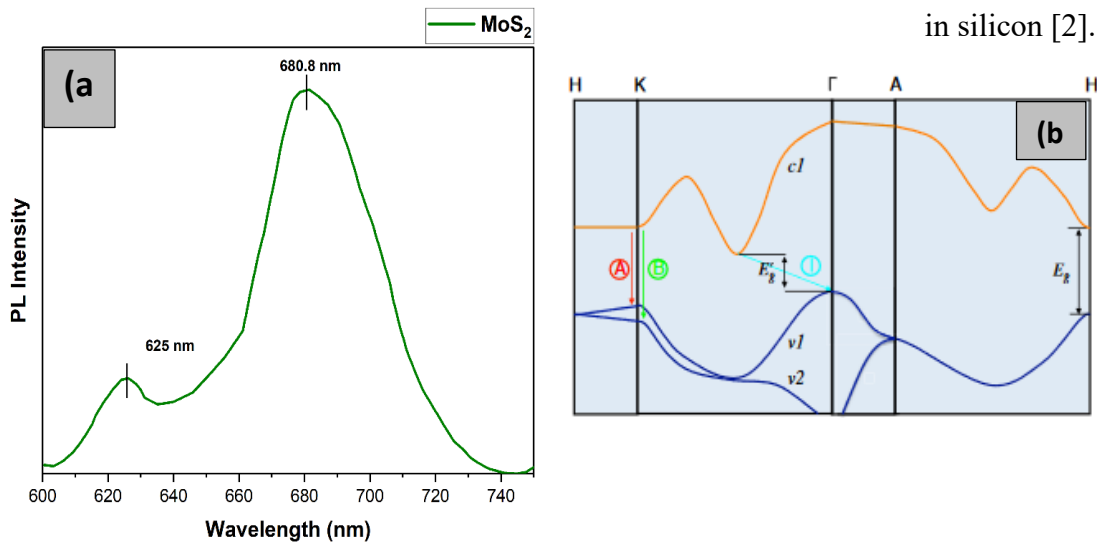

Figure 5.4: MoS₂ flake (a) PL Spectra & (d) Band Diagram [13]

5.3.3. Raman Spectroscopy

Regarding the use of Raman Spectroscopy, the use of relative frequency difference between the in-plane $E^1{}_{2g}$ and out-plane Raman Mode A_1g is a reliable method to count the number of layers and has been studied on a variety of substrate specially SiO_2. Based on the literature, following are the relative frequency differences that are calculated based on the number of layers of MoS_2 [2]: -

    i. 18.5-19.5 cm^{-1} for 1L

    ii. 23.0-24.0 cm^{-1} for 3L

    iii. 24.5-25.0 cm^{-1} for 6L

In the present case, peaks can be observed approximately at 404 cm^{-1} 385 cm^{-1} having a frequency difference of 19 cm^{-1} thus indicating the presence of single layered structured.
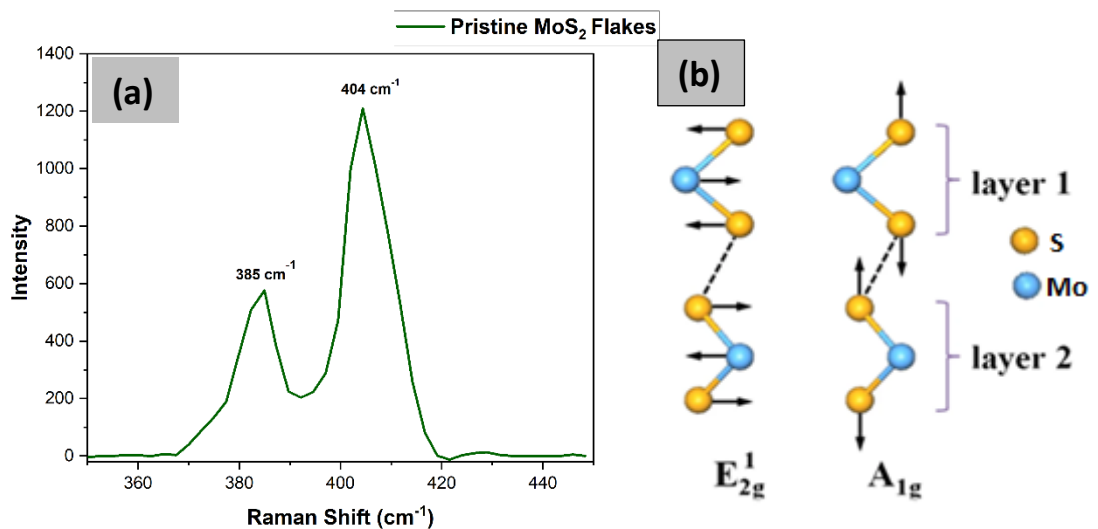
Figure 5.5: (a) Raman Spectroscopy of MoS_2 indicating the signature peak of A and B exciton of MoS_2 (b) Vibrational Mode of MoS_2 [3]

5.3. XRD Analysis

The size of the crystal, dislocation density and micro strain in the SnO_2 film and SnO_2 doped films are shown in Figure 5.6. along with their corresponding numerical values which are shown in Table 5.1 . Scherrer equation is used for the calculate of the crystallite size [4]

$$D = \frac{k\lambda}{\beta \cos \theta} \tag{5.7}$$

Where D is an average size of the ordered crystalline domain, k is a dimension less factor, λ is the X-ray wavelength, β is the full-width half-maxima (FWHM) and θ is the Bragg diffraction angle.

As indicated by the values mentioned in the table below, as the amount of dopant is increased, the crystallinity of the (110) and (101) phase has been improved along with the increasing intensity of the peaks up to 20% addition of MoS_2. After that it decreased for 30%. Inter-planar spacing, also known as d-spacing is actually the distance between two consecutive planes of an atom. It can be calculated by the Bragg's Law [5]

$$d = \frac{\lambda}{2 \sin \theta} \tag{5.8}$$

where d is the d-spacing and θ is the Bragg's angle which is the angle between the incident ray and the diffracting plane. It can be seen from values calculated for the d-spacing that there occurs no shift from the addition of dopant and has remained constant even with the increase of the added amount indicating that no ion or atom is displace in the lattice of SnO_2. Also, this could be due to the fact that the overall composite structure is dominated by the SnO_2, and the effect of the MoS_2 being the minority material on the crystal structure is not significant enough to cause a detectable peak shift. Therefore, the orientation of lattice is not affected since the spacing is neither increased nor decreased leading to constant values. The dislocation densities can be defined as length of dislocation lines per unit volume. It can be attributed to mismatch in the crystallite structure and are mathematically expressed and calculated by the following formula [6].

$$\delta = \frac{n}{D^2} \tag{5.9}$$

Where δ, n and D indicate dislocation densities, n is the mathematical factor normally taken 1 and D is the crystallite size calculated from Debye-Scherrer equation. As indicated in the Figure 5.6., the dislocation density has been improved

73

with the addition of flakes. This might be possibly due to the fact that the flakes have provided the nucleation site leading to growth of large crystal structure hence lowering the dislocation densities. However, as the concentration of dopant is increased, it is causing strain on the crystal growth leading to reduced crystallite size and crystal imperfection. Micro strain can be defined as the deviation of atom from their standard position in reference to their equilibrium position. This can be attributed to different reason such as point defects, dislocation near grain boundaries and porosities [7]. If the orientation of atom in the crystal lattice is in order this will lead to lower defects which in turn lead to lower micro strain. Micro strain is expressed by the following mathematical formula [8]

$$\varepsilon = \frac{\beta}{4 \times \tan \theta} \tag{5.10}$$

It can be seen that the with the addition of dopant, micro strain gradually increased up to 20% doping after which it slightly decreased at 30% indicating the disturbance created in the lattice due to the addition of MoS_2.

Table 5.1:Numerical Values of Crystallite Size, d-spacing, dislocation density and Micro-Strain obtained via XRD spectral fitting.

Sample Type	Crystallite Size (nm)	d-spacing (Å)	Dislocation density (lines/m^2)×10^{15}	Micro-strain (ε)×10^{-3}
SnO$_2$	11.26	3.36	7.89	14.03
SnO$_2$-10	11.44	3.36	7.64	13.81
SnO$_2$-20	13.11	3.36	5.81	12.04
SnO$_2$-30	12.84	3.36	6.07	12.30

Figure 5.7(b) shows the Cs-doped absorber layer on standard and doped ETL. All the peaks have shown to have typical perovskite tetragonal phase with the diffraction peaks appearing at 14.03°, 19.84°, 23.40°, 24.423°, 28.331°, 31.789°, 34.89°, 40.443° and 43.062° While the peaks corresponds to the following crystalline phase (110), (112), (211), (202), (220), (310), (312), (224) and (314) respectively for the above mentioned diffraction angle [9], [10]. Furthermore, the addition of dopant has

also supported the crystallinity of Perovskite film. The crystallite size have increased from intrinsic SnO_2 up to 20% SnO_2 and afterwards it decreased to 30% doped SnO_2 with perovskite deposited on 20% doped layer showing biggest crystallite size for
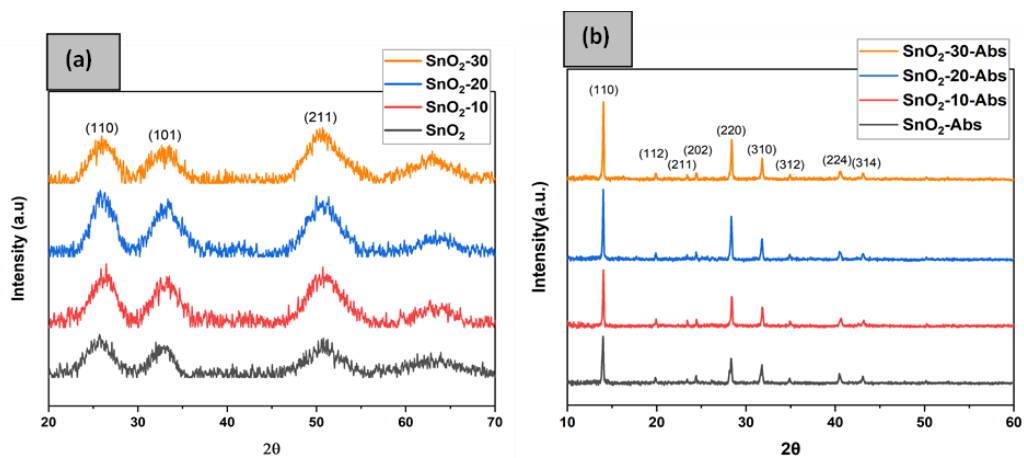
all phases. The reason of improved crystallinity can be attributed to passivation of defects and enhanced nucleation while the decrease in size may be the result of increased defect density and strain as indicated by the XRD of SnO_2 along with the agglomeration of flakes.

5.4.   Morphological Analysis

The effect of improvement in ETL can also be observed in the perovskite absorber layer since a well deposited electron transport layer contributes to improved morphological feature of perovskite absorber layer deposited on top of it. After that even though the film has shown much smoother morphology, large cracks have started to appear which can lead to reduced device performance due to higher recombinations rate.
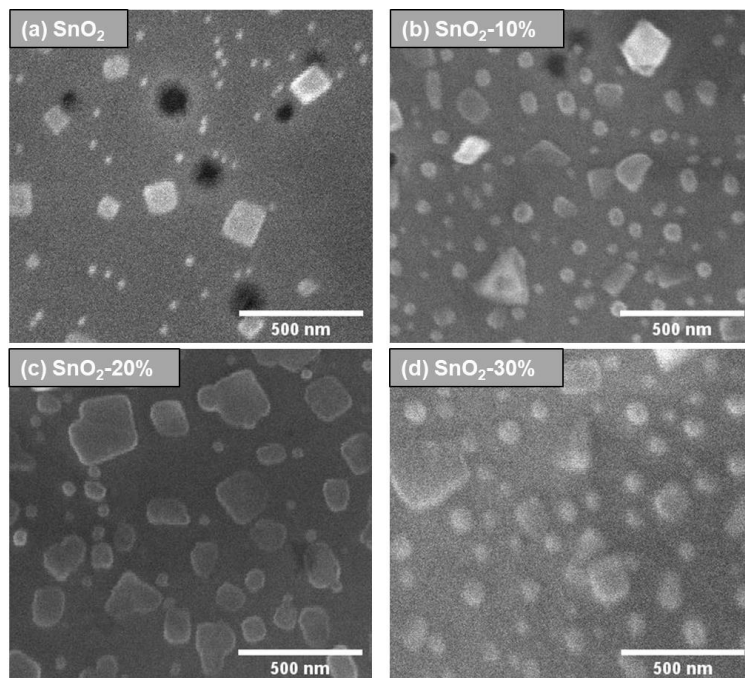
Figure 5.7: SEM images of (a-d) SnO_2 and SnO_2/MoS_2 composite
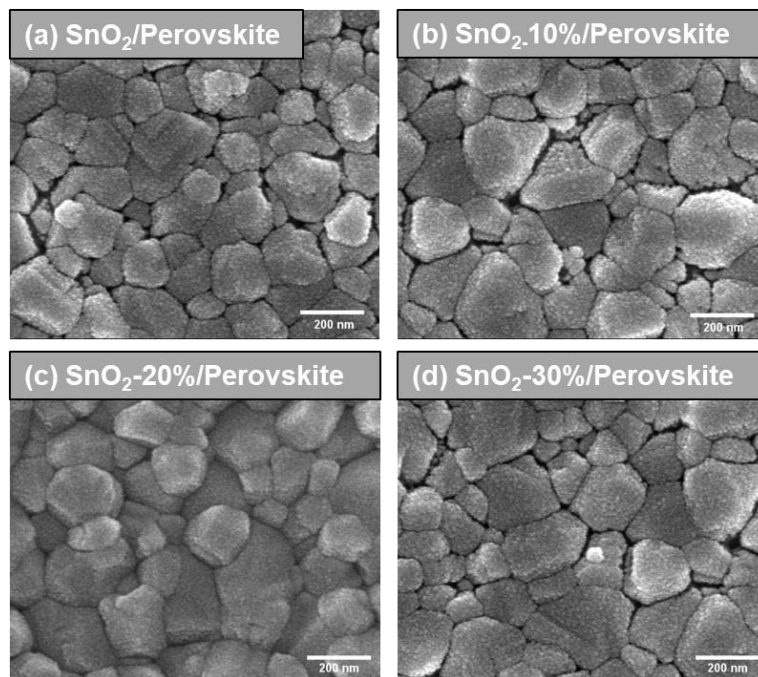

Figure 5.8: (a-d) Perovskite absorber layer on their respective ETL

5.5.   Effect of dopant on Transmittance

After addition of MoS_2 flakes solution in different concentrations, the solution was deposited on quartz substrate followed by UV testing to measure its absorption spectra. It can be seen as the percentage of flakes is increased, the transmittance of the layer started to decrease. There are various variables that affect the transmittance of the thin film. It includes crystal defects, grain size, thickness, and surface roughness. Transmittance of 10% is quite similar and near to that of pristine SnO_2. However, in the samples doped with MoS_2 in 20% and 30% (v/v %), the clear difference can be seen in comparison to the pristine SnO_2 Figure 5.9. However overall, all the layers have exhibited average good transparency ranging between 90.1% for pristine SnO_2 and 89% (SnO_2-30) in the visible region. This reduction in the thickness can be attributed to the crystal imperfection that has been increasing with the addition of MoS_2 and is indicated by the dislocation density. This leads to more increment in the phonon scattering which can be attributed to the increase crystal imperfection and reduced size of crystal.

In addition to this, by absorbing the SnO_2 and MoS_2 spectra one can see that in case of SnO_2 the transmittance remains fairly the same throughout the spectrum and it only absorbs in the UV region owing to its wide band gap. However, absorption by MoS_2 increases throughout the visible region and the band gap edge of the spectra is present near the UV region as indicated in Figure 5.9. This characteristic is adopted by their composite leading to decrease in the transmittance as the concentration of dopant is increased.
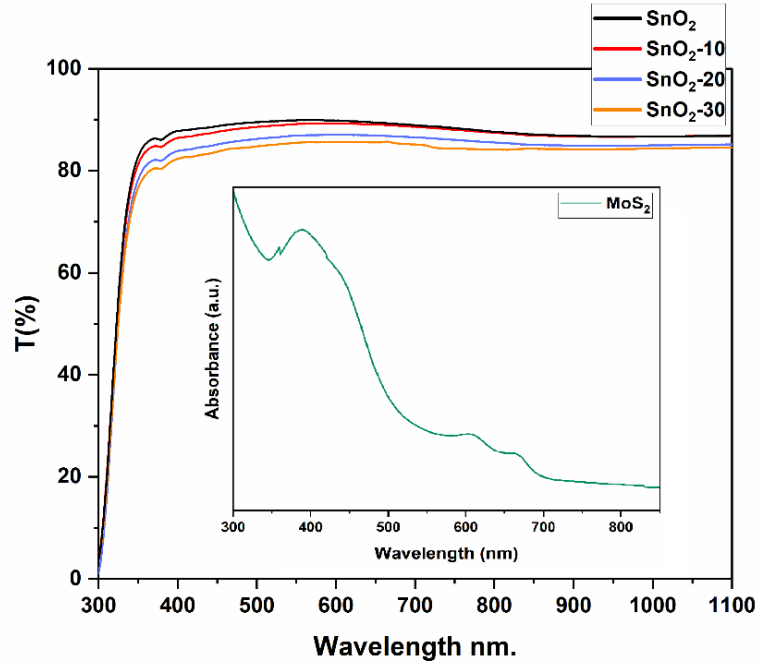
Figure 5.9: Transmittance Spectra of SnO2 and MoS$_2$ doped SnO$_2$

5.6. Effect on bandgap

In addition to the effect of dopant on the transmittance, the effect of dopant on the bad gap of the material is also studied with the help of the Tauc Plot. According to the Tauc Plot, the optical energy bandgap can be calculated by the following mathematical expression:

$$(\alpha h\nu)^m = A(h\nu - E_g) \qquad (5.11)$$

Where $h\nu$ is the energy of the incident photon, A is a constant which depends upon the type of transition that is taking place and E_g is the optical bandgap of energy while m is the exponential factor whose value depend upon the type of transition that is taking place. For direct transmission $m = 2$ and for indirect transmission $m = 1/2$. From the Tauc plot it can be seen that with the increase in the There is no huge difference when compared with the band gap of pristine SnO2, however a slight difference in the third digit after decimal can be seen from the Figure 5.10 as the

78

band gap varies from 3.993 eV for SnO$_2$, 3.911 eV for 10% doped, 3.844 eV for 20% doped and 3.841 eV for 30% doped SnO$_2$.
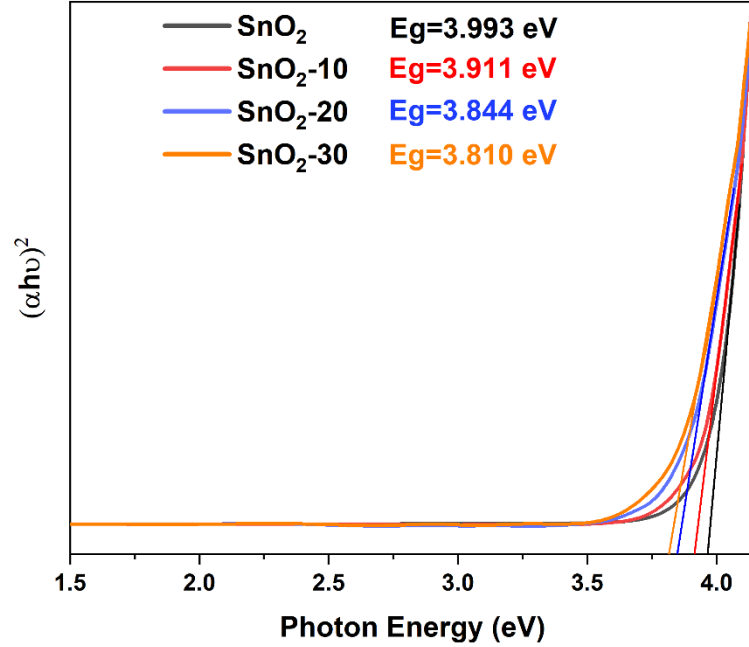

Figure 5.10: Tauc Plot of SnO$_2$ and MoS$_2$ doped SnO$_2$.

5.7.   Urbach Energy

Urbach Energy is the calculation of the quantitative measure of the energy disorder at the band edges of the semi-conductor material. The reason of the presence of Urbach energy can be attributed to the presence of passivation sites at the surface, structural disorder and imperfection in the structure. Mathematically, Urbach energy is calculated by the following mathematical equation having a relation between absorption coefficient (α) and photon energy (hν).

$$\alpha = \alpha_0 \left(\frac{h\nu}{E_U}\right) \tag{5.12}$$

Where α_0 and E_U are the constant and Urbach Energy respectively. The Urbach energy is calculated by plotting a linear relation between log (α) and hν and then taking the inverse of the slope which can be from Figure 5.11 (a). Furthermore from Figure 5.11 (b) the Urbach Energy values are calculated to be 291.92 meV, 294.1

meV, 295.82 meV and 297.69 for SnO$_2$, SnO$_2$-10%, SnO$_2$-20% and SnO$_2$-30% doped respectively.

The increase in the Urbach Energy can also be associated with the reduction in the bandgap
which might be due to the increase in the number of available energy states for electrons, which causes an increase in the number of localized states within the band gap. These localized states are responsible for the increase in Urbach energy. Furthermore, the increase in the electronic state near the band gap edge due to the increase in the Urbach energy also results in the increase in the absorption of Photon. This is also supported by UV-Vis where the decrease in the transmittance as a result of increase in doping .
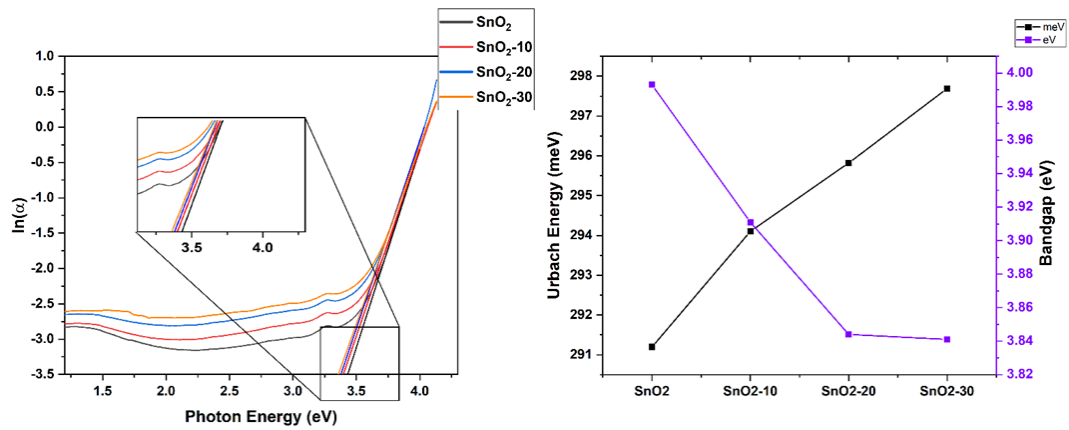
Figure 5.11 (a) linear plot between ln(α) and *hv* (b) plot shoowing the realtion between bandgap and Urbach energy

5.8.   Hall Effect

The Hall effect measurements were performed for different compositions of samples. The effect of doping on a number of different variables such as conductivity (σ), mobility (μ), sheet resistance (R$_s$) and charge carrier concentration (N$_b$) as a function of MoS$_2$ flakes is studied. It can be seen that the addition of doping has significantly affected all of the variables.

5.8.1. Effect on Charge Carrier Concentration

As the crystal size increases, the density of defects within the crystal can decrease. This is because larger crystals can accommodate more atoms per unit volume, which can lead to fewer defects such as dislocations, vacancies, and grain boundaries. These defects can act as scattering centers for charge carriers, reducing their mobility and decreasing the charge carrier concentration. By reducing the density of defects, higher N_b is achieved.

In addition to defect density, crystal size can also affect charge carrier concentration by altering the surface-to-volume ratio. A decrease in surface-to-volume ratio due to increased crystal size can lead to a reduction in surface states and surface recombination centers, which can also increase the charge carrier concentration.

$$n = 1/(q * R\_H * B) \tag{5.13}$$

where n is the electron concentration (in cm^{-3}), p is the hole concentration (in cm^{-3}), q is the charge of the charge carrier (in coulombs), RH is the Hall coefficient (in cm^3/C), and B is the applied magnetic field (in tesla).

5.8.2. Effect on Mobility

The mobility of the charge carriers can be calculated using the following formula:

$$\mu = VH/(B * j) \tag{5.14}$$

where μ is the mobility (in cm^2/Vs), VH is the Hall voltage (in volts), B is the applied magnetic field (in tesla), and J is the current density (in A/cm^2).

The addition of the dopant has initially caused the mobility to decrease. This is because initially mobility is influenced by the increasing number of charge carrier concentration. However, as the amount of MoS_2 is increased, has caused a reduction in the charge carrier concentration. This will eventually increase mobility.

5.8.3. Effect on Conductivity

The conductivity of the material can be calculated using the following formula:

$$\sigma = j/(E * d) \qquad\qquad (5.15)$$

where σ is the electrical conductivity (in S/cm), j is the current density (in A/cm^2), E is the electric field (in V/cm), and d is the thickness of the material (in cm).

Similar to the sheet resistance, the conductivity is also influenced by the change in the crystalite size. With the increase in the size there occur a reduction in defects as mentioned earlier. This causes increse in the conductivity thus facailitating the charge transport through the film and it decreases with the increasing concetartion.

5.8.4.   Effect on Sheet Resistance

The formula for sheet resistance in Hall effect measurements is:

$$Rs = (VH * d)/(IB) \qquad\qquad (5.16)$$

where Rs is the sheet resistance, VH is the Hall voltage, d is the thickness of the material, IB is the current density, which is the current per unit area applied to the material.
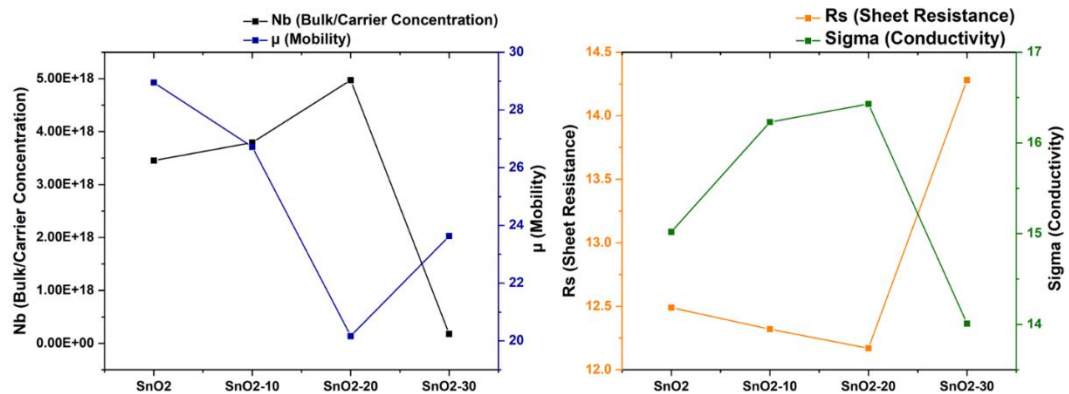
Figure 5.12: Hall Effect Parameters (a) Charge Carrier Concentration & Mobility (b) Sheet Resistance & Conductivity

The sheet resistance can be affected by the various variables. However, in the present case, the sheet resistance is mainly affected by the crystal size and defects present in the crystal structure. As indicated by the XRD results, addition of MoS2 has caused an increase in the crystal size, while lower the defects such as dislocation densities

and micro-strain. This causes a reduction in the sheet resistance for the composite. However, upon increasing the concentration from 20% to 30%, the crystal size is further reduced along with the increase in the defects in crystal structure. Furthermore, the reduction is crystal size is also associated with the increase in the surface to volume ratio which act as a trap center causing them to lose their mobility. All this will add up causing the increase in the sheet resistance.

5.9. Figure of Merit

Figure of merit (FOM) are the set of techniques or tools that are used to determine the effectiveness of a system, procedure, or technique. In the case of ETL, transparency is an important parameter that determines the effectiveness of the ETL by allowing the maximum amount of light to pass through it. To determine the effectiveness for ETL two of the most widely used method include Fraser & Cook and Haacke Method. However, the latter one is the much more improved method and is widely adopted throughout literature. For the calculation of FOM, the Haacke Method [11] is mathematically expressed as:

$$\phi = \frac{T^{10}}{R_{sh}} \tag{5.17}$$

where T represents the transmittance at 550 nm and R_{sh} represents the sheet resistance of the film that is calculated via Hall effect.
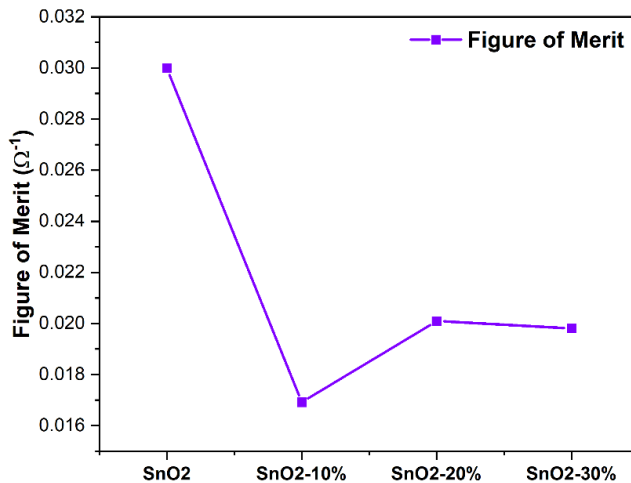

Figure 5.13: Figure of Merit as a function of MoS$_2$

FOM as a function of MoS_2 is shown in the

Figure 5.13. It can be seen from

Figure 5.13 for SnO_2 the value of FOM is 29.99×10^{-3} from where its value has decreased. However, among the doped sample the value for 20% sample has been higher increasing to 20.09×10^{-3} from 16.91×10^{-3} for 10% and then decreasing to 19.80×10^{-3} for 30%.

5.10. Effect on Photoluminescence Spectroscopy

PL was performed to study the charge carrier kinetics at ETL/Perovskite interface or efficient injection of photogenerated charge carriers from perovskite layer to ETL. The absorber layer was deposited on the top of the ETL layer with different doping concentrations. All the samples were excited with the excitation wavelength of 450 nm. Upon excitation, the perovskite absorber layer has shown its characteristics peak at 763 nm indicating significant recombination of electrons and holes to give off an intense peak.
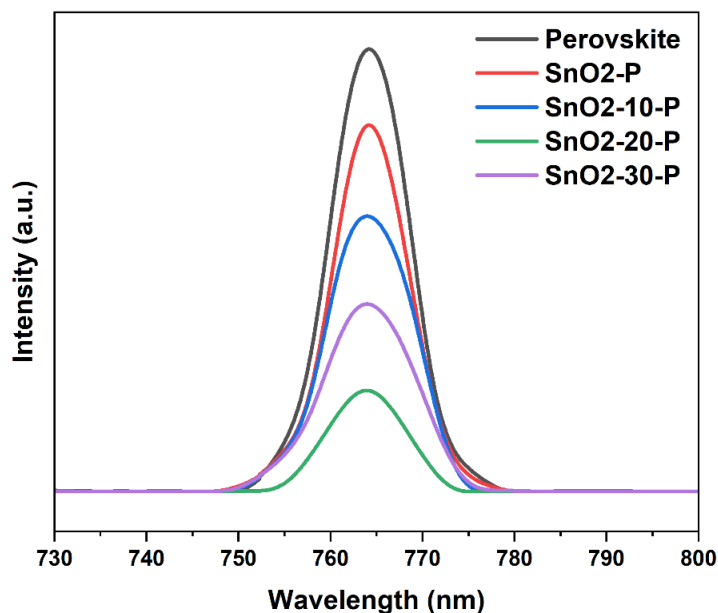

Figure 5.14: PL comparison of samples

As the perovskite was deposited on SnO_2, a reduction in the intensity of the peak can be observed which indicates that electrons are effectively transported to ETL.

Therefore, a lower number of electrons and holes are recombined thus giving off a less intense peak resulting in the quenching effect. Furthermore, as the dopants was added in SnO_2 in 10 (v/v %), 20 (v/v %), and 30 (v/v %), the intensity of the peak started decreasing from 10 (v/v %) to 20 (v/v %) and after which it again started increasing indicating that the most effective charge carrier recombination and less radiative recombination occurs at 20 (v/v%) in perovskite via doping concentration of MoS_2 flakes.

Another reason which can be attributed to the reduction in the radiative recombination in the perovskite film can be attributed to the mobility factor with the addition of MoS_2 flakes. The addition of flakes has allowed an increment in conductivity of the film thus benefiting the film overall. However, as the amount of dopant is increased from 30%, the additional flakes can not only provide recombination centers leading to the increase in the intensity of the peak in PL along with the reduction in the charge carrier concentration and conductivity along [12].

5.11.   IV of Half Cells: -

For IV testing, cells with different composition and different structure were prepared. Three different compositions are tried for Fabrication of Perovskite Solar Cell (PSC).

 i.Standard Composition-MAPbI$_3$

ii.10% Cesium doped MAPbI$_3$

• The ETL used is SnO_2 while the HTL and metal contacts is replaced by the mixture of Carbon and Graphite.
• The architecture of the devices is n-i-p.

5.11.1.1. IV of Half Cell with Standard Absorber Layer

For compositional engineering of perovskite absorber layer, Absorber layer was doped with Cesium to explore the role of cesium in providing stability for the solar cells regarding their ambient fabrication. Therefore, cells in three different

compositions were prepared. Three different compositions are tried for fabrication of PSC.

i.   Standard Composition-MAPbI$_3$.

ii.   10% Cesium Bromide (CsBr) doped MAPbI$_3$.

• The ETL used is SnO$_2$ while the HTL and metal contacts is replaced by the mixture of Carbon and Graphite.
• The architecture of the devices is kept n-i-p.

For IV testing, cells for both the discussed compositions were prepared in ambient. In the first case, the half cells were prepared with a standard absorber layer. Overall, the cell showed a decent efficiency with a decent efficiency of 3.1963%. Having an open circuit voltage of 0.6361 V, cells with standard absorber layer have displayed a tremendous, short circuit current density (J$_{sc}$) of 14.11 mA/cm^2. Also, FF is around 35.6%, which can be further improved with improvement in the energy level alignments.
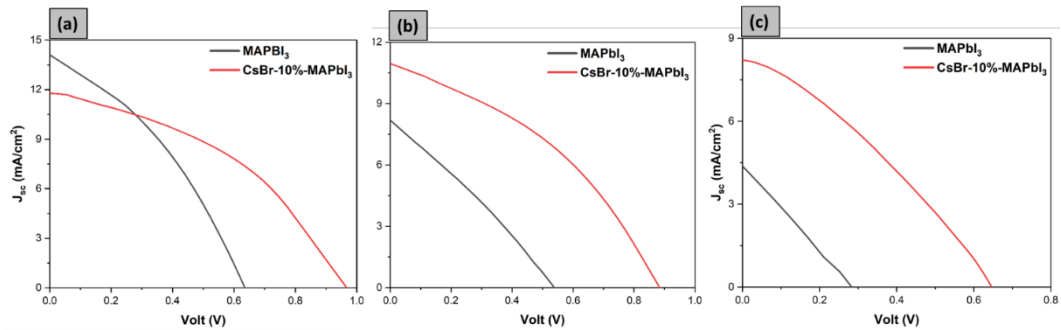
Figure 5.15: (a) First Test, Stability Test (b) After 48 hours and (c) After 120 hours

Table 5.2: First test of carbon based PSC

Sample Name	V$_{oc}$ (V)	J$_{sc}$ (mA/cm^2)	Fill Factor (%)	Efficiency (%)
MAPbI$_3$	0.6361	14.1082	35.6134	3.1963
CsBr-10%-MAPbI$_3$	0.967	11.7859	41.1957	4.6966

In the case of cells which were doped with 10% CsBr, the HTL free cells have displayed a good V$_{oc}$ which is better overall as compared to the standard absorber

layer. The champion cell has shown a dominant open circuit voltage of 0.967 V. This is due to the increase in the bandgap energy which occurs because of the addition of CsBr leading to higher V_{oc}. J_{sc} has been a bit lower, which might be attributed to the widening of bandgap. This results in the lower absorption of photons leading to less generation of charges thus reducing J_{sc}. However, the FF and efficiency has been improved significantly showing an impressive of 41.196% and 4.696% respectively. After their initial test, the cells were stored in ambient condition without encapsulation. Two stability tests for the cells were performed. The first test was performed after 48 hours, and the second test was performed after 120 hours. In the case of the first test, the efficiency of the cell with standard layer decreased by 60.84%. However, for 10% CsBr doped samples, the cells showed a degraded efficiency of 21.4069 % as compared to their initial efficiency values. Besides efficiency, all other parameters of CsBr based cells showed much more resilience to degradation as compared to their standard counterpart as mentioned in Table 5.3.

Table 5.3: First stability test of cell after 48 hours

Sample Name	V_{oc} (V)	J_{sc} (mA/cm^2)	Fill Factor (%)	Efficiency (%)
MAPbI$_3$	0.5379	8.1835	28.4268	1.2515
CsBr-10%-MAPbI$_3$	0.8828	10.8085	38.684	3.6912

In the case of the second stability test, the cells showed degraded performance by 90.09% for standard samples and 63.44% for 10% CsBr doped samples from their initial efficiency values. Besides efficiency, the CsBr based cells have been able to retain higher value of FF with and was able to secure an FF of 32.36% of FF even after 120 hours with only a decrement of 21.44% from their initial value. Compared to SAL, the cells were only able to retain an FF of 25.62% with a decrement of 28.04% after 120 hours. This degradation rate is much higher as compared to CsBr based solar cells. Furthermore, as far as J_{sc} and V_{oc} is concerned, there occurs only 8.29% decrement in J_{sc} and 68.9797% decrement in J_{sc} after 120 hours for CsBr based and SAL based cells respectively. Finally, for V_{oc} the decrement is 55.462%

for SAL while 32.47% decrement is observed for CBAL from their initial values after 120 hours.

Table 5.4: Second stability test of cell after 120 hours

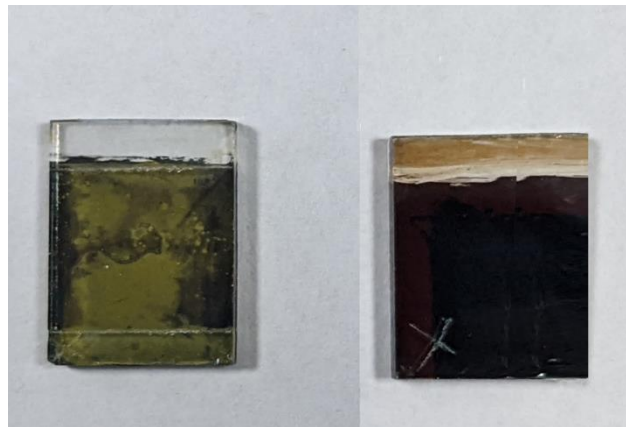| Sample Name	V_{oc} (V)	J_{sc} (mA/cm^2)	Fill Factor (%)	Efficiency (%)
MAPbI$_3$	0.2833	4.3764	25.6243	0.3178
CsBr-10%-MAPbI$_3$	0.6530	8.1236	32.3608	1.7167

Figure 5.16: (Left) Cell with MAPbI$_3$ layer and (Right) Cell with CsBr doped Absorber Layer after 120 hours of testing

References

[1]   J. Bahadur, A. H. Ghahremani, B. Martin, T. Druffel, M. K. Sunkara, and K. Pal, "Solution processed Mo doped SnO2 as an effective ETL in the fabrication of low temperature planer perovskite solar cell under ambient conditions," *Org Electron*, vol. 67, no. January, pp. 159–167, 2019, doi: 10.1016/j.orgel.2019.01.027.

[2]   A. Splendiani *et al.*, "Emerging photoluminescence in monolayer MoS2," *Nano Lett*, vol. 10, no. 4, pp. 1271–1275, Apr. 2010, doi: 10.1021/NL903868W/ASSET/IMAGES/MEDIUM/NL-2009-03868W_0005.GIF.

[3]   P. Hajiyev, C. Cong, C. Qiu, and T. Yu, "Contrast and Raman spectroscopy study of single-and few-layered charge density wave material: 2H-TaSe2," *Sci Rep*, vol. 3, 2013, doi: 10.1038/SREP02593.

[4]   A. L. Patterson, "The Scherrer Formula for X-Ray Particle Size Determination," *Physical Review*, vol. 56, no. 10, p. 978, Nov. 1939, doi: 10.1103/PhysRev.56.978.

[5]   L. R. B. Elton and D. F. Jackson, "X-Ray Diffraction and the Bragg Law," *Am J Phys*, vol. 34, no. 11, pp. 1036–1038, Nov. 1966, doi: 10.1119/1.1972439.

[6]   G. K. Williamson and R. E. Smallman, "III. Dislocation densities in some annealed and cold-worked metals from measurements on the X-ray debye-scherrer spectrum," *https://doi.org/10.1080/14786435608238074*, vol. 1, no. 1, pp. 34–46, 2006, doi: 10.1080/14786435608238074.

[7]   M. A. Mahmud *et al.*, "Controlled nucleation assisted restricted volume solvent annealing for stable perovskite solar cells," *Solar Energy Materials and Solar Cells*, vol. 167, pp. 70–86, Aug. 2017, doi: 10.1016/J.SOLMAT.2017.03.032.

[8]   L. H. Qian, S. C. Wang, Y. H. Zhao, and K. Lu, "Microstrain effect on thermal properties of nanocrystalline Cu," *Acta Mater*, vol. 50, no. 13, pp. 3425–3434, Aug. 2002, doi: 10.1016/S1359-6454(02)00155-6.

[9]   Y. Zhao and K. Zhu, "Charge Transport and Recombination in Perovskite (CH 3 NH 3)PbI 3 Sensitized TiO 2 Solar Cells," 2013, doi: 10.1021/jz401527q.

[10]   Y. Fan, H. Qin, W. Ye, M. Liu, F. Huang, and D. Zhong, "Improving the stability of methylammonium lead iodide perovskite solar cells by cesium doping," *Thin Solid Films*, vol. 667, pp. 40–47, Dec. 2018, doi: 10.1016/J.TSF.2018.10.001.

[11]   G. Haacke, "New figure of merit for transparent conductors," *J Appl Phys*, vol. 47, no. 9, pp. 4086–4089, Sep. 1976, doi: 10.1063/1.323240.

[12]   D. Wang *et al.*, "MoS2 incorporated hybrid hole transport layer for high performance and stable perovskite solar cells," *Synth Met*, vol. 246, pp. 195–203, Dec. 2018, doi: 10.1016/J.SYNTHMET.2018.10.012.

[13]   K. F. Mak, C. Lee, J. Hone, J. Shan, and T. F. Heinz, "Atomically thin MoS2: A new direct-gap semiconductor," *Phys Rev Lett*, vol. 105, no. 13, p. 136805, Sep. 2010, doi: 10.1103/PHYSREVLETT.105.136805/FIGURES/4/MEDIUM.

Chapter 6

Conclusion and Future Recommendations

The following chapter concludes the outcomes extracted from this research. Furthermore, some future recommendations are also proposed to work on the following topic.

6.1 Conclusion

In conclusion, introduction about the different types of solar cell and particularly Perovskite solar cell has been explained following a comprehensive literature review on low temperature and surface modified SnO2 based ETL. Afterwards operational procedure and principles of various characterization equipment were explained. Then the process for the preparation of materials and for there is further explained.

As for the results, solution processing method was used for the synthesis of SnO_2 which was later mixed with the MoS_2 flakes in 10 v/v%, 20 v/v%, and 30 v/v%. The samples were subjected to various characterization techniques including XRD, SEM, PL, UV-Vis, Raman, Hall Effect and IV curve measurement. XRD indicates that SnO_2 has been successfully synthesized with the improvement in the crystallinity of the film with 20% being the best quantity. Furthermore, morphological studies have also suggested the improvement in the grain size for Perovskite deposited on SnO_2-20. UV-Vis has indicated a drop in transmittance and reduction in the bandgap due to the addition of flakes while Hall Effect has shown improvement in the N_b, conductivity, and reduction in the mobility and resistivity for 20% sample. Finally different types of cells based on the difference of their absorber layer including standard $MAPbI_3$ and cesium doped mix halide and mix

cation perovskite carbon based solar cells were prepared with 10% Cs based cells showing the best efficiency.

6.2   Future Recommendations

Following are the recommendations that can be used for the improvement in the stability of solar cell:

i.   Synthesis method other than solution processing should be explored for the synthesis of ETL along with ensuring the smooth their deposition.

ii.   Characterization equipment such as SEM, XPS and UPS can be used further to enhance the quality of research and to bring insights and further detail to attention.

iii.   Regarding the carbon paste, their deposition and preparation particularly regarding viscosity in recipe is further needed to be optimized to improve the charge extraction capability of the layer.

iv.   Standard procedures for the deposition of the solar cell need to be adopted for high efficiency device fabrication.

v.   The quality of materials must be ensured before being brought to their use for synthesis and fabrication.

Journal Publication

Characterizing the Synergistic Effects of SnO$_2$-MoS$_2$ Nanocomposite Electron Transport Layers for Perovskite Solar Cells

Muhammad Salik Qureshi[a], *Nadia Shahzad[a], Saad Nadeem[a], Sana Mehmood[a], Abdul Sattar[b], Naseem Iqbal[a], Sehar Shakir[a], Muhammad Imran Shahzad[c], Muhammad Usman Nawaz[a]

[a]*U.S.-Pakistan Centre for Advanced Studies in Energy (USPCAS-E), National University of Sciences & Technology (NUST), H-12 Sector (44000) Islamabad, Pakistan*

[b]*Energy Materiaux Telecommunications Research Center, Institut National de la Recherche Scientifique (INRS-EMT), Quebec, Canada*
[c]*Nanosciences and Technology Department (NS&TD), National Centre for Physics (NCP), 44000 Islamabad, Pakistan*

*Corresponding Author's Email: nadia@uspcase.nust.edu.pk

Abstract

The Electron transport layer (ETL) plays a crucial role in the performance of perovskite solar cells (PSC). Charged with the task of electron extraction and delivering them to their respective electrode, they play a vital role in enhancing the overall performance of the solar cell. Several materials particularly metal oxide (MO) and their composites have been tested for this role. Tin Oxide (SnO$_2$) and its composites have shown superior properties that have proven crucial for enhancing the performance of solar cells by improving the charge extraction properties of the layer. Therefore, this paper presents the study of a composite of SnO$_2$ with the pristine nano flakes of Molybdenum Disulfide (MoS$_2$), a new emerging material for solar cell application. The addition of 20% (v/v) MoS$_2$ in SnO$_2$ has not only improved the crystallinity of SnO$_2$ but also resulted in enhanced and larger grain size for the perovskite absorber layer. In addition, the flakes also cause an increase in the charge carrier concentration and conductivity of the film. Furthermore, due to the incorporation of flakes the charge carrier recombinations at the ETL/perovskite interface was also reduced leading to superior charge transportation showing that

the SnO_2 and MoS_2 composite will be a suitable option as an ETL for development of PSC.

Keyword: Electron transport layer, perovskite solar cells, SnO_2-MoS_2 composite, Ambient Fabrication